Journal of Low Temperature Physics, Vol. 129, Nos. 5/6, December 2002 (© 2002)

Morphology and Growth Kinetics of ^{3}He Crystals below 1 mK

Viktor Tsepelin[†a], Harry Alles[†], Alexei Babkin[†b], Reyer Jochemsen[‡], Alexander Ya. Parshin[§], and Igor A. Todoshchenko[†]

[†] *Low Temperature Laboratory, Helsinki University of Technology, P.O. Box 2200, FIN-02015 HUT, Helsinki, Finland*
[‡] *Kamerlingh Onnes Laboratory, Leiden University, P.O. Box 9504, 2300RA Leiden, The Netherlands*
[§] *P.L. Kapitza Institute for Physical Problems, ul. Kosygina 2, 117334 Moscow, Russia*

The shapes as well as the growth and melting properties of bcc-^{3}He single crystals have been investigated with a low temperature Fabry-Pérot interferometer. Eleven types of facets were clearly identified during slow crystal growth at the temperature of 0.55 mK, where the solid is in the antiferromagnetically ordered u2d2 phase. The growth rates of the individual facets have been measured and the results indicate significant growth anisotropy. The observed linear dependence of the growth velocity on the driving force shows that facets grow due to the presence of screw dislocations, while the step velocity is limited by the spin wave velocity due to the strong interaction of the moving step with magnons in the solid. The measured growth rates of the facets and the assumed growth mechanism gave us the unique opportunity to obtain the step free energies for ten different types of facets observed during a single growth sequence. The dependence of the free energy of the step on the step height is compared with predictions of the weak- and strong-coupling models. Our results suggest that ^{3}He crystals have rather strong coupling of the liquid/solid interface to the crystal lattice and that the step-step interactions are of elastic origin.

PACS numbers: 67.80.-s, 68.08.-p, 68.35.Rh, 81.10.Aj

1. INTRODUCTION

Most of the crystals seen in nature have a polyhedral shape with smooth flat facets and sharp edges in between. These facets correspond to high-symmetry crystallographic orientations and are the result of the formation of crystals in a distant past. The growth dynamics and the equilibrium shape of ordinary crystals can usually be studied only at elevated temperatures close to their melting point. Therefore due to large differences in entropy of the solid and the adjacent melt or vapor phases and the finite thermal conductivities of these bulk phases, the dynamics of ordinary crystals is very slow. Nevertheless, equilibrium shapes with rounded (rough) areas between flat facets have been observed with microscopic metal crystals,[1–3] some organic materials[4] and ice crystals,[5] for instance.

In equilibrium situation, any smooth surface part of the crystal, a facet, should become rough (rounded) at high enough temperature, at the so called roughening transition, first considered by Burton, Cabrera and Frank[6] (see also Ref. 7). It has to be pointed out that, due to the reasons mentioned above, the roughening transitions can hardly be studied quantitatively even in the systems, where thermodynamic equilibrium can be reached.

The helium crystals, which exist at low temperatures and high pressures, are exceptional compared with ordinary crystals because their growth dynamics as well as the equilibrium shape can be studied in a wide temperature range along the melting curve down to $T = 0$. At low enough temperatures, where the latent heat of crystallization is negligible and the surrounding superfluid phase has good thermal conductivity, the growth and equilibrium of helium crystals are practically independent of heat and mass flow considerations. Thus helium crystals present a good model system where the internal properties of the liquid/solid interface can be studied.

The equilibrium shape of ^{4}He crystals can be obtained relatively easily - below 0.5 K the relaxation time of the rough surface is a few milliseconds.[8] The studies on the equilibrium and dynamic properties of ^{4}He crystals have yielded important information on the equilibrium crystal shape as well as the growth mechanisms.[8–10] In the hexagonal close packed ^{4}He three types of facets, (0001), $(1\bar{1}00)$ and $(1\bar{1}01)$, have been observed with their roughening transitions at 1.3 K, 0.9 K and 0.36 K.[11–15] The roughening transition of the (0001) facet has been studied most extensively[10] while the third facet, $(1\bar{1}01)$, has been observed only during growth.[15] No more than three types of facets have been detected in ^{4}He down to 2 mK.[16]

Nozières and Gallet[17] have developed the renormalization approach to the roughening transition, which has been shown to be in a good agreement with several experiments near the roughening transition of the (0001) facet

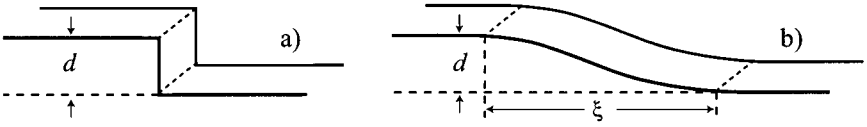

Fig. 1. Profile of an elementary step in the *a*) strong- and *b*) weak-coupling limit.

in ^{4}He. In ^{4}He the so called weak-coupling limit has been found to be valid which means that the liquid/solid interface is weakly coupled to the crystal lattice.[7,18]

Consider a facet on the interface with the surface energy γ_0 at $T = 0$. The profile of the elementary step on the facet could be sharp (Fig. 1a) or broad (Fig. 1b). The first case corresponds to the strong-coupling limit, where the interface is pinned by the lattice potential, thus the step energy β_0 (per unit length) is roughly equal to the surface energy of the additional area: $\beta_0 \sim \gamma_0 d$, where d is the step height. This situation occurs more or less on the vacuum/solid interface of metals;[19] in spite of the anisotropy (a particular facet can have steps in different directions with different step energies) the ratio $\beta_0/\gamma_0 d \approx 1$.

In the weak-coupling situation sketched in Fig. 1b (the case of ^{4}He), the distribution of the step over a number of lattice spacings will reduce the step energy, and $\beta_0/\gamma_0 d \ll 1$ and $\xi/d \gg 1$, where ξ is the step width. Experimentally it has been found that for the (0001) facet in ^{4}He $\xi \simeq 8\ d$,[20] or even $\xi \simeq 16\ d$ [21] with $\beta/\gamma d \simeq 0.057$.[20] Since the zero-point motion in ^{3}He is larger than in ^{4}He, it has been suggested[18] that the coupling of the interface to the solid lattice in ^{3}He would be even weaker than in ^{4}He.[1]

The equilibrium shape of ^{3}He crystals has been observed only in the vicinity of the melting curve minimum, $T_m = 320$ mK, where the latent heat vanishes.[22] In this temperature range the crystals are nicely rounded and no facets are present since T_m is above all roughening transitions. Away from the melting curve minimum the latent heat increases and ^{3}He crystals behave like ordinary crystals, *i.e.*, have very slow dynamics.[23,24] Only well below the Néel temperature, $T_N = 0.93$ mK, where the spins of solid ^{3}He are antiferromagnetically ordered and the surrounding liquid phase is superfluid, ^{3}He crystals are expected to show fast dynamics similar to ^{4}He crystals at much higher temperatures.[25]

When we started our optical experiments with ^{3}He crystals, three types

[1]Note that near the roughening transition, due to critical fluctuations, ξ tends to infinity (see Ref. 7). In this sense, the coupling is always weak in the vicinity of the roughening transition.

of facets had been observed in this system. First, facets of the (110) type were seen in the body-centered cubic (*bcc*) ^{3}He crystals at $T \approx 80$ mK by Rolley *et al.*[26] Later two other types of facets, (100) and (211), were identified when growing the ^{3}He crystals at $T \approx 2$ mK from the superfluid phase.[24] The growth of faceted ^{3}He crystals had been measured below T_N using Nuclear Magnetic Resonance (NMR) techniques[27,28] and direct optical observations.[29] The growth velocities of the individual facets had not been measured and only an average growth rate of ^{3}He crystals was reported.[29] Even though the growth rate of the crystals in the narrow channels in the experiments of the Kyoto group[28,30] were most likely due to growth of a single facet, it is not known which facet was at the liquid/solid interface. All performed measurements had shown similar growth rates with rather weak temperature dependence. Nomura *et al.*[28] had observed a linear dependence of the growth velocity on the driving force and they had associated it with growth of facets in the regime of the saturated step mobility.

In this paper the results of our experiments with ^{3}He crystals are presented which were obtained with the help of a Fabry-Pérot multiple-beam interferometer, built inside the nuclear demagnetization cryostat. Short reports of this work have been published earlier.[32–34] We were able to identify altogether eleven different types of facets during growth of the ^{3}He crystals at our lowest temperature of 0.55 mK.[32,33] We measured also the growth rates of individual facets and observed significant anisotropy.[34] Melting processes with much faster dynamics were studied as well, and the results suggest that the measured growth velocities of facets were not limited by the processes in the bulk phases, but are due to intrinsic mechanisms taking place at the interface. One of our most remarkable conclusions is that ^{3}He has surprisingly stronger coupling of the liquid/solid interface to the crystal lattice than ^{4}He, in spite of larger zero-point fluctuations in ^{3}He.

The paper is organized as follows: in Section 2 the equilibrium crystal shape and the roughening transition are considered first. The theoretical part describes also the weak- and strong-coupling limits as well as the growth mechanisms of rough and smooth surfaces. Descriptions of our optical setup and experimental techniques are given in Section 3 which is followed by the explanation of our data analysis in Section 4. Our experimental results on faceting and growth dynamics of ^{3}He crystals are presented and discussed in Section 5.

2. THEORETICAL BACKGROUND

2.1. Equilibrium Crystal Shape and Roughening Transition

The equilibrium shape of a crystal surrounded with liquid is determined by the free energy per unit area of the interface between the two bulk phases, the surface tension α. The minimization of the total free energy over the whole crystal surface yields the equilibrium crystal shape. The condition for the phase equilibrium at a given point of the interface is the Herring equation:[35]

$$\delta p \left(\frac{\rho_s}{\rho_l} - 1 \right) = \left(\alpha + \frac{\partial^2 \alpha}{\partial \phi_1^2} \right) \frac{1}{R_1} + \left(\alpha + \frac{\partial^2 \alpha}{\partial \phi_2^2} \right) \frac{1}{R_2}. \tag{1}$$

Here δp is the pressure of the bulk liquid calculated from the nominal equilibrium pressure for a planar interface, ρ_s and ρ_l are the densities of the solid and liquid phases, R_1 and R_2 are the two principal radii of the surface curvature and ϕ_1 and ϕ_2 are the corresponding angular coordinates. The expression $\gamma \equiv \alpha \delta_{\mu\nu} + \partial^2 \alpha / (\partial \phi_\mu \partial \phi_\nu)$ is the surface stiffness tensor.

If the surface tension of a crystal would be isotropic, then the equilibrium crystal shape would be a perfect sphere in the absence of gravity. However, a crystal consists of a lattice of atoms and the binding energy between the neighboring atoms varies for different crystallographic orientations, which results in the anisotropy of the surface tension. It was shown by Landau[36] that at $T = 0$ the surface tension α of a crystal is a very unusual function of the surface orientation: it is continuous, but has a cusp for every rational (*i.e.*, with integer Miller indices) orientation, and the larger the Miller indices, the smaller the cusp. The appearance of facets, smooth flat faces on the crystal surface, is a direct result of this unusual behavior of α. The equilibrium facet size is therefore proportional to the value of this surface tension cusp for a given orientation. As for Eq. (1), one may treat it as follows: a cusp in α means infinite surface stiffness and Eq. (1) yields then zero curvature, *e.g.*, a facet.

According to Landau, as there is an infinite number of different crystallographic orientations, the surface of an ideal crystal is covered with an infinite number of facets (so called "devil's staircase" phenomenon). In his paper Landau neglected the surface fluctuations, both thermal and quantum. It was shown later by Fisher and Weeks[37] (see also Refs. 38,39) that quantum fluctuations do not destroy the crystal faceting, thus at $T = 0$ limit any real crystal (classical or quantum) should be entirely faceted and have many different types of facets on its surface.

As temperature increases and the thermal fluctuations blur the cusp in the surface tension for a certain crystallographic orientation, the correspond-

ing facet disappears. Each type of facets has its own roughening transition temperature T_R given by[37,7]

$$k_B T_R = \frac{2}{\pi}\sqrt{\gamma_{\|}\gamma_{\perp}}\, d^2, \tag{2}$$

where k_B is the Boltzmann constant, d is the interplanar distance (the height of an elementary step on the facet) and $(\gamma_{\|}, \gamma_{\perp})$ are the principal components of the surface stiffness for a given surface orientation. Both components should be measured at the temperature above but close to the expected transition temperature for that part of the surface. In the *bcc* lattice $d_{hkl} = \frac{1}{2}a(h^2+k^2+l^2)^{-1/2}$, where a is the lattice constant and $\langle hkl \rangle$ is the reciprocal lattice vector.[40]

A well-defined excitation on a facet is an elementary step, a linear defect that separates the facet into two parts which differ in height by one atomic spacing. The step has a finite width ξ, which is determined by its internal structure and the amplitude of the surface fluctuations — both zero-point and thermal. If ξ is small, on the order of the lattice constant a, the step is strongly localized by the lattice potential — it is the strong-coupling limit (see Fig. 1a); respectively, in the weak-coupling limit ξ is large (Fig. 1b).[7]

The characteristics of steps determine the properties of the vicinal surfaces which are tilted by a small angle with respect to the main ("primary") facets so that the distance between steps is large compared to their width ξ. These properties are different in the strong- and weak-coupling limits which are discussed in the next two Sections.

2.1.1. Strong-coupling limit

In the strong-coupling limit we can follow Landau[36] and consider a vicinal surface of a *bcc* crystal as a distribution of steps on a primary facet (to be definite, we take the (100) facet with the $(N10)$ vicinals, where N is large). These primary steps can be considered to behave as isotropic strings with linear tension per unit length β_{100}, the step free energy. The surface stiffness of a vicinal surface is determined then by the value of β_{100} and the interaction between steps at long distances. The most long-ranged are the elastic[41] and entropic[42] interactions which both depend on the distance as $1/x^2$. At low temperatures which we are interested in (the mK-range), the entropic interaction is relatively weak. The energy of the elastic interaction U (per unit length) can be written in the form[41]

$$U(x) = \frac{f^2}{E}\left(\frac{d_{100}}{x}\right)^2 \cdot \frac{2}{\pi}\left(1-\sigma^2\right), \tag{3}$$

where d_{100} is the step height, E is the Young modulus, σ is the Poisson ratio, f is a function of the elastic strain produced by the step (with the same order of magnitude as the surface tension α) and x is the distance between steps; for vicinal surfaces of the type $(N10)$, $x = Nd_{100}$.

The density of steps and thus the surface tension both depend on the tilt angle of the vicinal surface. This angle can be changed by rotation around two principal axes, along and perpendicular to the steps and these are the corresponding principal values of the surface stiffness $\gamma_{||}$ and $\gamma_{\perp}$ in Eq. (2).[7] Straightforward calculation yields

$$\gamma_{||} = \frac{2\pi(1-\sigma^2)}{Ed_{100}} \frac{f^2}{N}, \quad \gamma_{\perp} = \frac{\beta_{100}}{d_{100}} N. \tag{4}$$

This result is valid only if the vicinal surface itself is rough, *i.e.*, there is no cusp in the surface tension at the corresponding surface orientation. Thus the temperature should be higher than the roughening transition temperature T_{N10} for a given vicinal surface and lower than T_R for the primary facet. The value of T_{N10} could be calculated using Eq. (2) and the obtained values of $\gamma_{||}$ and $\gamma_{\perp}$ from Eq. (4). However, one should keep in mind that in the vicinity of a roughening transition critical fluctuations start to develop. As a result, at the very transition point γ will be somewhat renormalised compared with Eq. (4).[7,17] Therefore one can make only a rough estimate of T_{N10} as

$$k_B T_{N10} \approx \sqrt{\frac{\beta_{100}}{E}} f \frac{d_{N10}^2}{d_{100}}, \tag{5}$$

where d_{N10} is the interplanar distance between parallel $(N10)$ planes or, in other words, the height of a secondary step (note that in the *bcc* lattice $d_{N10} = a/N$ for odd N and $d_{N10} = a/2N$ for even N).[43] Similar estimates of roughening temperatures are valid for other families of vicinal facets.

At temperatures below T_{N10}, the $(N10)$ facets appear and the secondary steps become well defined. The energies of these steps can be found by the method originally used by Landau,[36] who made calculations for the case of the van der Waals interaction between steps. Let us have a set of parallel steps with height d_{100} on a primary facet (100) with all distances between steps equal to x, except one which is larger by $\Delta x \ll x$ (see Fig. 2).

Let the interaction energy between steps m and n be $U_{mn} = 1/x_{mn}^2$,

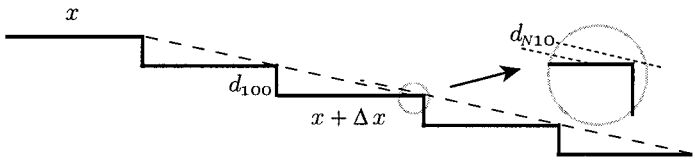

Fig. 2. Secondary step on the crystal surface.

then the change of the total energy due to the shift of steps by Δx is

$$\begin{aligned}\Delta U^{+} &= \sum_{m>0,n\leq 0} (x_{mn} + \Delta x)^{-2} - x_{mn}^{-2} \\ &= \sum_{m>0,n\leq 0} -2\frac{\Delta x}{x_{mn}^{3}} + 3\frac{(\Delta x)^{2}}{x_{mn}^{4}} \\ &= -\frac{\pi^{2}}{3}\frac{\Delta x}{x^{3}} + 3\zeta(3)\frac{(\Delta x)^{2}}{x^{4}},\end{aligned} \tag{6}$$

where $\zeta(3) = 1.202...$ For a similar configuration of steps, but with a shift Δx of opposite sign the change of the total energy becomes

$$\Delta U^{-} = \frac{\pi^{2}}{3}\frac{\Delta x}{x^{3}} + 3\zeta(3)\frac{(\Delta x)^{2}}{x^{4}}. \tag{7}$$

The sum of these two expressions is exactly the energy of a pair of secondary steps with opposite signs. Taking the interaction energy in the form of Eq. (3), one obtains for the energy of one secondary step

$$\beta_{N10} = \frac{6}{\pi}\zeta(3)\frac{(1-\sigma^{2})}{E}\frac{f^{2}}{d_{0}^{2}(\Delta x)^{2}}d_{N10}^{4}. \tag{8}$$

In the *bcc* crystals this derivation is literally valid only for an odd N ($N = 2k + 1$). The vicinal facet with an even N ($N = 2k$) is a mixture of the $(2k + 1\ 1\ 0)$ and $(2k - 1\ 1\ 0)$ facets. However, Eq. (8) is correct also for such facets as well as for other families of facets like $(N\ 1\ 1)$, $(N\ 2\ 1)$, *etc.* Moreover, this result is valid for the families of facets which are vicinal to the other primary facets like (110), (211), *etc.* if d_0 is the height of a primary step and Δx is the minimal nonzero shift of this step. Here is, for further references, a short list of these values:

for the (100) facet ($d_0 = a/2$), $\Delta x = a$ and $a/\sqrt{2}$ for the $(N\ 1\ 0)$ and $(N\ 1\ 1)$ families, respectively;

for the (110) facet ($d_0 = a/\sqrt{2}$), $\Delta x = a/2, a/\sqrt{2}$, and $a\sqrt{3}/2$ for the $(N\ N\ 1)$, $(N + 1\ N\ 0)$, and $(N + 1\ N\ 1)$ families, respectively.

Note also, that we have calculated only energies of steps which are parallel to the primary steps. For other orientations these energies should be

somewhat different. However, in the following we will neglect this anisotropy and discuss our experimental data in terms of a simple theory of the isotropic spiral growth. We will neglect also possible anisotropy in the value of f.

In general we conclude from the strong-coupling model (the narrow step width) that the step energy depends on the step height as a fourth power: $\beta \propto d^4$. It is assumed that the steps are well separated, meaning that the model may not be valid for facets with small Miller indices, *i.e.*, for primary facets.

2.1.2. Weak-coupling limit

For the weak-coupling situation with wide steps the step energy is expected to be significantly reduced (with respect to γd), and also the dependence on the step height will change. Following Nozières[7] we can estimate the values of β and ξ by writing $\beta \sim d\sqrt{\gamma V}$, where V is the energy barrier which pins the liquid/solid interface to the crystal lattice and separates the neighboring equilibrium positions of the interface. If the effective width of the interface l is large, V is exponentially small. Assuming that l is approximately constant for all surface orientations, one may write $V \sim \gamma \exp(-l/d)$ and

$$\beta \sim d\gamma \exp(-l/2d). \tag{9}$$

The value of ξ can then be found by noticing that for each facet the product $\xi\beta$ is roughly independent of temperature below T_R:[7]

$$\xi\beta \sim k_B T_R. \tag{10}$$

Although Eq. (10) is only derived for temperatures close to T_R, it has been shown that in ^{4}He the extrapolation of this relation to $T = 0$ gives good results.[44] The actual temperatures of the roughening transitions in ^{3}He are not known, but these can be estimated by substituting the surface stiffness value into Eq. (2). The surface stiffness of ^{3}He crystals has been measured only at high temperatures where no facets exist and γ is almost isotropic and temperature independent, $\gamma = \gamma_0 \approx 0.06$ erg/cm^2.[22] When the temperature approaches T_R (from above), γ increases due to critical fluctuations as mentioned in the previous Section. However, in the weak-coupling approximation this effect is small. Thus the value of $\gamma = \gamma_0$ may be used to estimate T_R for various facets with the exception of vicinal surfaces with very high Miller indices ($N > \xi/d$) which have steps well separated. Indeed, in contrast to a rough interface of a general orientation, the surface stiffness of a vicinal surface is highly anisotropic [see above, Eq. (4)]; accordingly, its roughening transition temperature is given by Eq. (5). This is valid as long

as the distance between steps ($x \sim Nd$) remains large compared with the step width ξ. In the opposite case, on the vicinal surfaces with rather small Miller indices the steps cannot be well defined any more, and such a vicinal surface behaves as a rough surface of a general orientation, with $\gamma \approx \gamma_0$ and with almost no renormalization of γ close to T_R. Following Rolley *et al.*[20] we will distinguish vicinal surfaces of these two types as stepped and rough, respectively.

The available experimental data on β, ξ and l in ^{3}He are very poor. In fact, there is only one rather indirect estimation of β, made by Rolley *et al.*,[22] $\beta_{110} \approx 1.2 \cdot 10^{-11}$ erg/cm, which gives $\xi_{110} \approx 100\ d_{110} \approx 3 \cdot 10^{-6}$ cm. With this value of ξ, only surfaces with very high Miller indices, like (N N 1), ($N+1$ N 0) *etc.* with $N > 100$ may be called stepped, all other surfaces are rough, except the facet (110) itself (and, of course, the other facets if they exist at a given temperature).

An independent, but also indirect estimate of β and ξ in ^{3}He can be obtained as follows. First one can calculate l in ^{4}He, using Eq. (9) and the measured values of $\beta_{0001} = 4.2 \cdot 10^{-10}$ erg/cm and $\gamma_{0001} = 0.245$ erg/cm^2 for the (0001) facets.[20,18] The result is $l/d_{0001} = 5.7$.[45] Due to the larger amplitude of zero-point fluctuations one expects in ^{3}He a somewhat larger value; so it is reasonable to assume $l/d_{110} = 7...8$.[46] Using this value one obtains $\beta_{110} = 3...5 \cdot 10^{-11}$ erg/cm, which is not very far from the result by Rolley *et al.*[22] Note that Eq. (9) predicts a very fast decrease of β for higher order facets.

If these estimates are valid, one may use $\gamma = \gamma_0$ in the calculation of T_R for most of the orientations of interest. Among the facets observed experimentally before the present study, (110), (100) and (211), Eq. (2) gives the lowest T_R for the (211) facet, $T_{211} \approx 85$ mK, and more than 1000 different types of facets should exist at 0.7 mK depending on the anisotropy of the surface tension. However, with such small values of β the equilibrium sizes of facets are expected to be very small. According to Landau,[36] the equilibrium size L_{hkl} of a facet is proportional to β_{hkl}:

$$L_{hkl} \approx \frac{\beta_{hkl} R}{d_{hkl} \gamma_0}, \tag{11}$$

where R is the characteristic size of a crystal. For the (110) facet Eq. (11) gives $L \sim 10^{-2} R$, and much smaller values for higher order facets. This is the reason why some authors[22,24] have suggested that in ^{3}He the facets are too small to be observed in equilibrium, even the (110) facets.

Thus, if ^{3}He crystals would behave according to the weak-coupling model, the direct optical observation of facets in equilibrium is hardly possible, and all previous observations of faceting in ^{3}He must have been done

in a non-equilibrium situation (*i.e.*, during growth), which is in fact the case.[26,22,24] This means that, in order to observe higher order facets, one should go even further from equilibrium. However, then one runs into another problem which may prevent the observation of facets. During the non-equilibrium situation of growth the weak-coupling theory predicts dynamic roughening which results in disappearance of facets even at temperatures well below T_R.[7,17] The corresponding chemical potential difference $\Delta\mu$ that causes the facets to disappear can be estimated as

$$\Delta\mu \sim \frac{\beta^2}{\gamma d^3}. \tag{12}$$

Equation (12) presents a rather severe condition. One can calculate the overpressure δp above which a particular facet should dynamically roughen. Taking $l/d_{110} = 7...8$, one obtains $\Delta\mu \sim 1$ mbar for the (110) facet and $\Delta\mu \sim 10^{-5}$ μbar for facets like (510).

To conclude, the weak-coupling model predicts an exponential dependence of the step energy on the step height. That behavior would be very interesting to observe since it has never been observed directly in any system. The applicability of the weak-coupling model to ^{4}He was obtained from various properties of a single facet, and the step energies of the other two observed facets in ^{4}He are not known. However, it is obvious that in the case of weak coupling the observation of higher order facets in ^{3}He is practically impossible both in equilibrium and during growth of the crystal, and the weaker the coupling, the smaller the number of different facets which could be observed.

2.2. Crystal Growth

2.2.1. Mobility of a rough surface

Growth of a crystal can be viewed as an addition of new particles to the sticking sites. Thermal or quantum fluctuations ensure a certain density of such sites on rough surfaces and thus the growth of a rough interface does not have a threshold.[47] The growth rate v of such an interface is proportional to the chemical potential difference $\Delta\mu$ (per unit mass) driving the growth:

$$v = k_{\text{int}}\Delta\mu, \tag{13}$$

where k_{int} is the intrinsic growth coefficient of the liquid/solid interface. The chemical potential difference between the liquid and solid phases in the case of a flat interface can be expressed as

$$\Delta\mu = \frac{\rho_s - \rho_l}{\rho_s \rho_l}\delta p, \tag{14}$$

where δp is the pressure change in the liquid with respect to the equilibrium melting pressure value.

Direct measurements of the intrinsic growth coefficient by means of melting or growing a crystal are difficult because the release of latent heat L and the thermal impedances of the bulk liquid and solid phases $Z_l(Z_s)$ and of the interface usually mask it completely. Experimentally accessible is only the effective growth coefficient $k_{\rm eff}$:

$$\frac{1}{k_{\rm eff}} = \frac{1}{k_{\rm int}} + \frac{\rho_s}{T}\frac{Z_l Z_s R_K}{Z_l + Z_s + R_K}\left[\frac{(TS_l - \lambda)^2}{Z_s} + \frac{(TS_s - \lambda)^2}{Z_l} + \frac{L^2}{R_K}\right]. \quad (15)$$

Here S_l and S_s are the entropies of the liquid and solid, R_K is the Kapitza resistance of the liquid/solid interface and λ determines the distribution of the latent heat, released or absorbed at the interface, over the two bulk phases.[23] Unfortunately, the thermal impedances of the bulk phases make the effective growth coefficient dependent on the cell geometry and the results of different experiments cannot be easily compared.

The intrinsic mobility of the liquid/solid interface of ^{3}He has been measured only at the minimum of the melting curve, where the latent heat vanishes and the result was $k_{\rm int} = 0.18$ s/m.[23,49] In all other experiments the thermal impedances have played a major role, and the intrinsic growth coefficient of ^{3}He crystals has been predicted to be measurable only below 0.2 mK.[25]

A rather strong temperature dependence of the growth coefficient has been observed in the temperature region of 0.44...0.73 mK by the NMR measurements.[28] The solid was melting much faster at lower temperatures, unfortunately, it was not possible to measure that quantitatively. Later optical experiments, conducted at 0.7 mK, have reported a value of $k_{\rm eff} = 2.3 \cdot 10^{-4}$ s/m.[29]

2.2.2. Growth of facets

Facets grow layer by layer and this process is slow since some mechanism is required for the creation of sites where atoms can stick to. As a result, the dissipative processes in the adjacent bulk phases do not have a significant influence on the growth properties, and in Eq. (15) the first term is dominant.

In dislocation-free crystals, the growth of the facets is determined by the nucleation rate of new atomic layers and is highly non-linear with respect to the applied chemical potential difference. At high temperatures the thermal energy is the most significant and two-dimensional nucleation of terraces becomes favorable on the facets. The growth velocity v of a facet growing

due to the two-dimensional nucleation mechanism can be expressed as[50,51]

$$v \sim (\Delta\mu/k_BT)\exp\left(-\frac{\pi\beta^2}{3d\rho_s\Delta\mu k_BT}\right). \tag{16}$$

At low temperatures the thermal fluctuations become weaker and growth due to the quantum nucleation mechanism with even stronger dependence on the driving force $[\exp(\Delta\mu)^{-2}]$ will dominate.[52]

In the presence of screw dislocations spiral growth is the main growth mechanism at any temperature except very close to the roughening transition temperature where β vanishes.[50] In the *bcc* lattice screw dislocations can have only two types of Burger's vectors $\vec{b}$: $\langle\pm\frac{1}{2},\pm\frac{1}{2},\pm\frac{1}{2}\rangle$, and $\langle\pm1,0,0\rangle$, $\langle0,\pm1,0\rangle$, $\langle0,0,\pm1\rangle$ since dislocations with other Burger's vectors have too high elastic energies and are unstable.

When a dislocation crosses the crystal surface, a step with an atomic height is produced. Strictly speaking, this is true only for the (110) facet, where $\vec{b} = \langle\frac{1}{2},\frac{1}{2},\frac{1}{2}\rangle$ or $\langle1,0,0\rangle$ and the step height $a/\sqrt{2}$ corresponds exactly to the interplanar distance. On all other facets dislocations can produce a varying number of steps. For example, on the (100) facet the dislocation with $\vec{b} = \langle\frac{1}{2},\frac{1}{2},\frac{1}{2}\rangle$ produces one step with the elementary height $a/2$, while $\vec{b} = \langle1,0,0\rangle$ produces a step with double height a. However, such step is unstable and two steps with the elementary height are actually created.

The theory of spiral growth of ^{4}He crystals[16] turned out to be somewhat more complicated than the classical spiral growth theory, due to the effects of step inertia and quantum localization of steps, which the theory had to take into account. However, in ^{3}He both effects may be neglected since the step velocity v_s is restricted to a relatively low critical velocity v_c, when the step mobility suddenly decreases. The growth velocity v of a facet in the subcritical regime is

$$v = \frac{\mu d^3}{19\beta}\frac{(\rho_s-\rho_l)^2}{\rho_l^2}K\delta p^2, \tag{17}$$

where μ is the step mobility defined as $\mu = v_s/(\rho_s d\Delta\mu)$, and K is the number of steps produced by one dislocation.

In ^{3}He the step mobility has not been measured. At $T < T_N$, this mobility can be estimated, taking into account the two main dissipative processes which contribute to the step resistivity $1/\mu$, namely the scatterings of (1) magnons from the solid and (2) quasiparticles from the superfluid at their collisions with a moving step.

In the limit of low temperatures, the magnon wavelength is large and the magnon contribution $1/\mu_{\rm mag}$ can be calculated using the scattering cross-section of a long wave at a rigid step, similarly to the case of the ^{3}He impurity

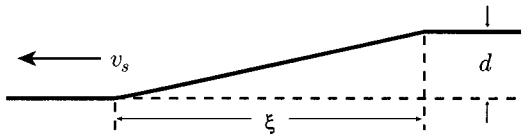

Fig. 3. Profile of a moving step (ξ – step width, d – step height).

in ^{4}He.[53] The result is

$$\frac{1}{\mu_{\rm mag}} = \frac{8\zeta(5)}{\pi^2}\frac{d^2 k_B^5 T^5}{\hbar^4 c^5}, \tag{18}$$

where $\zeta(5) = 1{,}037...$, $\hbar$ is the Planck constant and c is the magnon velocity.

In the strong-coupling limit, this result should be valid practically up to T_N. In contrast, in the weak-coupling limit, where the step width ξ is large, there is an intermediate temperature interval, $\hbar c/k_B\xi < T < T_N$, where this contribution can be estimated as

$$\frac{1}{\mu_{\rm mag}} \sim \frac{d^2}{\xi}\frac{k_B^4 T^4}{\hbar^3 c^4}. \tag{19}$$

In these estimations a specular (100%) reflection at the interface was assumed and the anisotropy in the magnon velocity was neglected.

In contrast to magnons, the characteristic wavelength of quasiparticles is short, $\lambda \sim a$, and their scattering cross-section is unknown. One can roughly estimate the contribution of quasiparticles $1/\mu_{\rm qp}$ by assuming that the step is a macroscopic object with a profile shown in Fig. 3 which moves in superfluid ^{3}He with velocity v_s. Then the drag force acting on this object can be obtained by the method used by Fisher *et al.*[54] in their calculation of the force acting on the vibrating wire. At $d \sim a$ this approach should give a correct order of magnitude. Assuming $\xi >> a$ (weak coupling) and specular reflection of quasiparticles, one obtains in the limit of low step velocities (compared with the thermal velocities of the quasiparticles)

$$\frac{1}{\mu_{\rm qp}} = \frac{16}{9\pi^3}\frac{p_F^4 d^2}{\hbar^3 \xi}\exp(-\Delta/k_B T), \tag{20}$$

where Δ is the superfluid energy gap and p_F is the momentum of quasiparticles. At higher velocities this mobility increases (see Ref. 54). As an order of magnitude estimate, this calculation should be valid also in the strong-coupling limit by taking $\xi \approx a$. Numerically this contribution is small compared with the magnon contribution at all temperatures below T_N, see Eq. (18).

In Section 2.1.2 it was concluded that significant driving forces (overpressures) may be needed to observe large enough facets in ^{3}He, which means that we have to consider the situation with rather large step velocities. The growth rate of facets is adequately described by Eq. (17) until the step velocity exceeds some critical velocity v_c and the step mobility suddenly decreases due to a Cherenkov-type creation of excitations. In this regime the growth velocity does not depend on the step mobility anymore, resulting in a linear dependence of the facet growth velocity on the overpressure δp:

$$v = \frac{v_c d^2}{2\pi\beta} \frac{\rho_s - \rho_l}{\rho_l} \delta p K. \tag{21}$$

In ^{3}He the lowest critical velocities are, first, the magnon velocity c and second, the pair-breaking velocity v_{pb}. In low magnetic fields, both are approximately 7 cm/s.[55,56] The effect of magnons and quasiparticles on the step mobility depends on the strength of their coupling to the step motion. For magnons rather strong coupling is expected because the moving step directly touches and disturbs spins in the solid next to the interface and thus radiates effectively spin waves when $v_s > c$. It means that such a Cherenkov radiation significantly suppresses the step mobility at $v_s > c$.

For quasiparticles the situation is expected to be different due to their large momentum and, at the same time, the large value of the effective width ξ of the step. Similarly to the case of rotons in ^{4}He,[16] at $v_s \sim v_c = \Delta/p_F$ the Cherenkov radiation of quasiparticles is exponentially weak in ^{3}He and proportional to $\exp(-\pi\xi\Delta/\hbar v_s) \sim \exp(-\pi\xi p_F/\hbar)$, becoming significant only at much higher step velocities.

3. EXPERIMENTAL TECHNIQUES

3.1. Experimental Setup

Most of the optical studies with helium crystals have been carried out using conventional optical cryostats with several sets of windows.[8,11,12] In such configuration the temperatures below 20 mK cannot be reached because of thermal radiation to the sample through the windows. The optical studies at submillikelvin temperatures became possible after a novel technical approach was put forward by the two research groups in Leiden[57] and in Helsinki.[58] Both groups had their optical instruments, including an imaging system, confined inside the 4-K vacuum jacket of the cryostat. Owing to this improvement, the external heat loads caused by the "hot" optical windows were avoided or at least greatly reduced.

To study the morphology and growth kinetics of ^{3}He crystals below 1 mK we have modified the experimental setup which was used for optical investigations on ^{4}He crystals by the Helsinki group.[16] The heart of our optical setup is a Fabry-Pérot multiple-beam interferometer which is described in detail in Section 3.3. A sketch of our latest experimental arrangement inside the nuclear demagnetization cryostat is depicted in Fig. 4. The first cooling stage of our cryostat is a commercial dilution refrigerator Oxford 600.[59] The original mixing chamber of the refrigerator was replaced with a custom-made one which has the effective heat-exchange area of 600 m^2. During performance tests the refrigerator showed the base temperature of 5 mK. It was possible to maintain the cooling power of 5.3 μW with the circulation rate of 500 μmole/s at 15 mK. A melting-curve thermometer and a primary ^{60}Co nuclear-orientation thermometer were used to monitor the temperature of the mixing chamber during these performance tests.

Submillikelvin temperatures were produced by the means of an adiabatic nuclear demagnetization technique. Our nuclear stage contains 104 moles of high-purity copper with the effective amount of 36.6 moles in the magnetic field of 8 T. It has a typical "Helsinki" design: a copper rod with a few dozen parallel 1 mm slits along the main axis cut by a spark cutter. Before installation the copper stage was carefully annealed in the vacuum oven at 960 °C for 100 hours. The nuclear stage is fixed to the mixing chamber by four 15 cm long tubes made of Al_2O_3. The adjustable thermal link between the mixing chamber and the nuclear stage is achieved with a superconducting heat switch made of four aluminium foils. The aluminium foils were connected to the copper pieces by diffusion bonding. The measured total electrical resistance of the heat switch was 44 nΩ at 4.2 K.

A platinum NMR thermometer was built to monitor the temperature of the nuclear stage. The platinum sensor is a brush of 1100 high-purity 25 μm Pt-wires, arc-welded to a silver holder. The Pt-thermometer was calibrated at 6...25 mK against the nuclear orientation thermometer.

In the present setup the incoming and outgoing optical arms are separated, which simplified the design and the optical adjustments of the interferometer. Several optical components like the beam expander, the beam splitter and the light dumper, are housed below the mixing chamber to minimize the optical path between the end of the fiber and the interferometer. All these components are thermally anchored to the cold plate ($T \approx 70$ mK) in order to reduce the heat load to the mixing chamber.

The design of our experimental cell is illustrated in Fig. 5. Conceptually the cell consists of two parts: from the compression cell and the optical chamber. In experiments with solid ^{3}He the pressure in the cell cannot be regulated through the fill line below $T_m = 320$ mK because of the melting

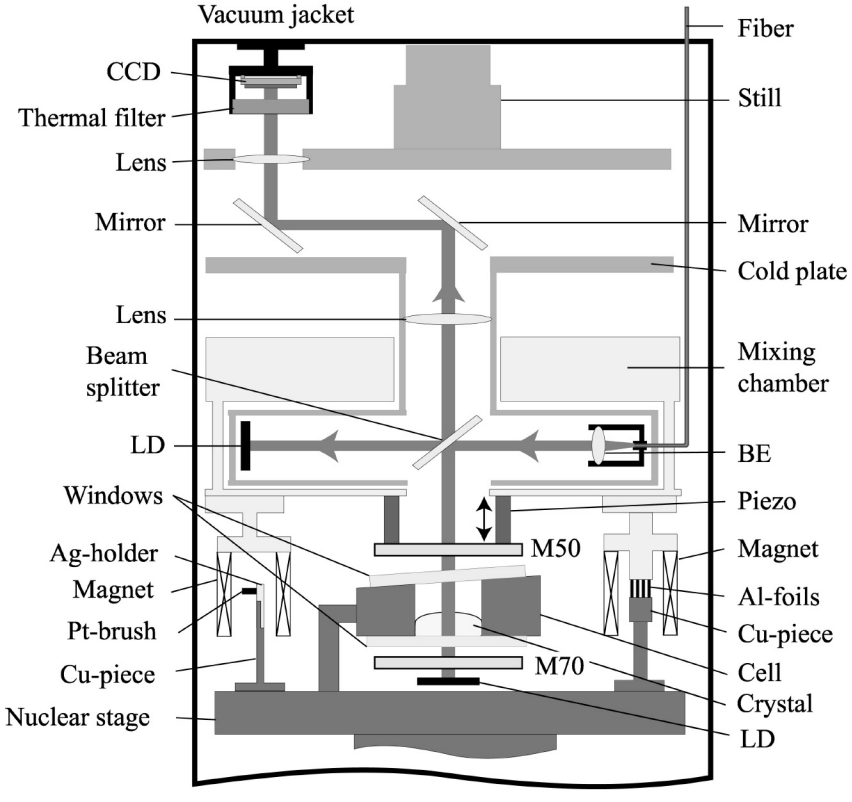

Fig. 4. Layout of the setup for optical studies on ^{3}He crystals: (CCD) Charge Coupled Device, (LD) light dumper, (BE) beam expander, (M50) and (M70) are the interferometer mirrors with 50% and 70% reflectivities, respectively.

curve minimum at that temperature: the fill line has a plug of solid ^{3}He. A usual way to solve this problem is to use a hydraulic amplifier (so called Pomeranchuk-type cell) made of two BeCu bellows. We use ^{4}He as the actuator media, and the amplification gain of our compressional chamber is about 3.4. A controlled flow of ^{4}He was used to pressurize ^{3}He in the cell.

The crystals were nucleated in the optical part of the cell which is a cylindrical copper body ($\varnothing = 16$ mm, $h = 12$ mm) sealed off by two fused-silica windows with antireflection coatings on all optical surfaces. In the center of the cell is a ring made of Stycast 1266[60] ($\varnothing = 12$ mm) which prevents the direct flow of liquid to the crystal in the observable part of the cell. The ring serves also as a holder for a nucleator which is placed just outside the field of view. It is a tungsten-tip to which a high voltage can be

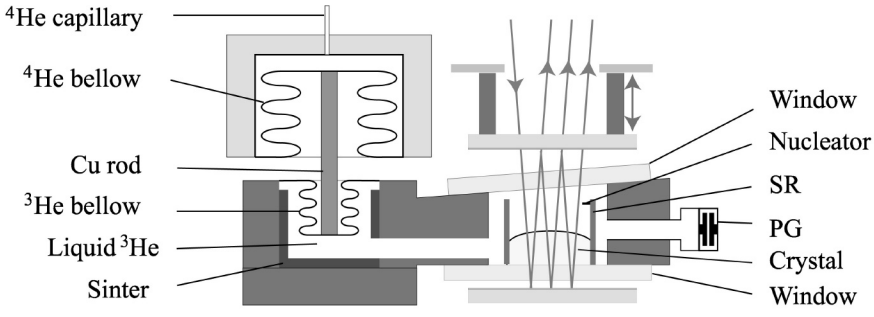

Fig. 5. Sketch of the experimental cell and the interferometer: (PG) pressure gauge, (SR) Stycast ring.

applied.

The experimental cell is thermally connected to the nuclear demagnetization stage by a copper rod ($\varnothing = 10$ mm) with the length of 10 cm. The total volume of the cell is about 13 cm^3 and this volume can be changed up to 8% by the means of BeCu bellows system. Liquid ^{3}He is cooled via a silver sinter with the effective area of about 50 m^2.

The pressure of ^{3}He was monitored by the capacitance measurements of a Straty-Adams type strain gauge[61] implemented in the cell. The BeCu membrane of the gauge is 0.4 mm thick and has a diameter of 9 mm. On each cooldown from room temperature the pressure gauge was calibrated at about 1 K against the Bourdon gauge. The resolution of our pressure gauge is a few μbar at 35 bars when measured with an AH 2500A capacitance bridge.[62] The pressure and the flow rate of ^{4}He were measured at room temperature.

3.2. Temperature Calibration

The melting curve of ^{3}He is known quite accurately and the measurements of the equilibrium melting pressure of ^{3}He are often used as a secondary thermometer. We calculated the temperature in our cell from the equilibrium melting curve pressure using Adams' temperature scale.[63]

The temperature calibration, or to be more explicit, the dependence of the gauge capacitance C versus pressure p was checked after every demagnetization. A small crystal was kept in the cell during warm up. The capacitances at three fixed points on the melting curve of ^{3}He were used to determine the fit parameters a and b for the pressure gauge ($p = a/C + b$). The typical pressure trace obtained during warm up is presented in Fig. 6. First, the slope of the melting curve changes at $T = 0.93$ mK due to the

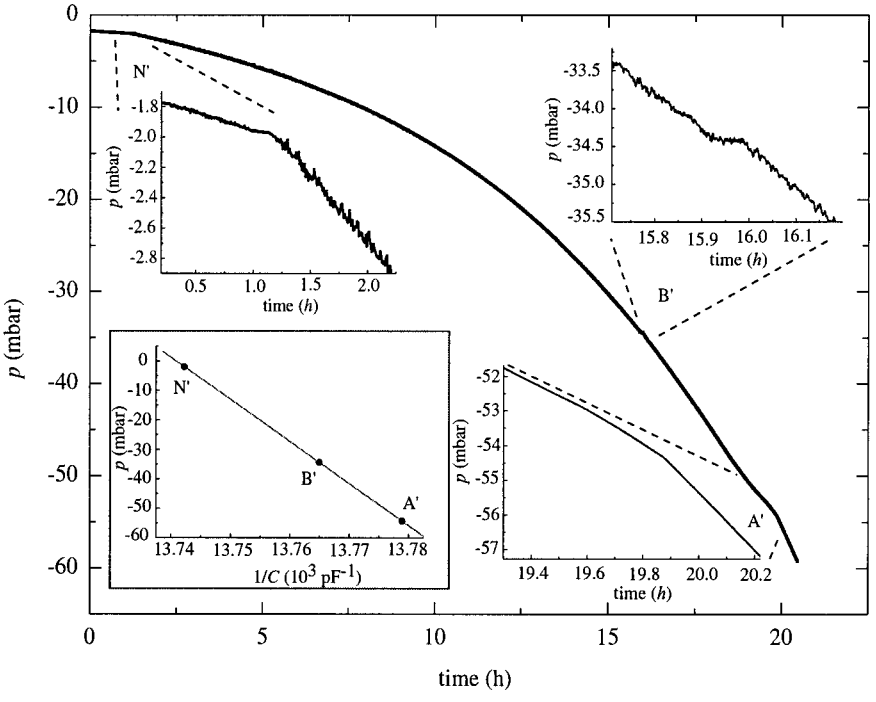

Fig. 6. Fixed points in the ^{3}He pressure trace for the temperature calibration during warm up. Inserts show in detail the A', B' and N' transitions (see text). Zero of the pressure axis corresponds to the melting curve value at $T = 0$.

Néel transition (N') in solid ^{3}He:[63] from the antiferromagnetically ordered state it becomes paramagnetic, *i.e.*, disordered. Next transition (B') can be recognized as a flat step on the pressure trace (first order transition), when superfluid B-phase becomes A-phase at $T = 1.93$ mK. The last fixed point (A') is again the slope change of the melting curve at $T = 2.5$ mK, where superfluid A-phase becomes normal liquid. The calibration was not checked on the cooldown due to the supercooling of the A-phase.

3.3. Fabry-Pérot Multiple-Beam Interferometer

Instead of the two-beam Fizeau interferometer[16] which was used in the previous setup in order to study the ^{4}He crystals we designed and built a Fabry-Pérot multiple-beam interferometer[64] with a phase shift facility into

our nuclear demagnetization cryostat. Unlike the two-beam interferometer which has a very small angular resolution, the multiple-beam interferometer allows to observe the whole crystal shape as well as the fine details on the liquid/solid interface. It reduces also significantly the imaging light intensity, which is very essential at ultra low temperatures. Compared with the two-beam path interferometry, the multiple-beam interferometry has a simpler experimental implementation and sharper fringes.

The He-Ne laser beam, which is guided into the cryostat through a single-mode optical fiber and enlarged by the beam expander to a diameter of 8 mm, enters the interferometer after the reflection from a 50% beam splitter as seen from Fig. 4. The interferometer is formed by two parallel mirrors placed above and below the cell. To improve the rigidity of the adjustments, these mirrors were located as close to the optical part of the cell as possible, the distance between the mirrors is about 45 mm. The top mirror of the interferometer can be shifted in a vertical direction by the means of a cylindrical piezo-electric crystal to which the mirror is attached.[64] The piezo transducer and the mirrors are thermally connected to the mixing chamber.

The light passes the upper mirror and undergoes multiple reflections between the mirrors as illustrated in Fig. 5. The interference pattern, formed by the interfering beams, is reflected back through the top mirror and is focused by the objective and the periscope to a remote CCD-sensor[65] inside the vacuum can. A thermal filter from CaF_2 with an 8 mm thickness cuts off the thermal radiation of the CCD-sensor (operated at about 65 K) from entering the cell. The "unused" beams are absorbed by light dumpers made of black velvet.

Our slow-scan CCD-sensor has 575×383 light-sensitive elements (pixels) and that yields the horizontal resolution of about 15 μm while the vertical resolution in the interface position achieved with our multiple-beam interferometer is a few micrometers. Crystal surfaces with a slope of up to 70° with respect to the bottom mirror of the interferometer can be identified.

4. ANALYSIS OF INTERFEROGRAMS

In the case of an ideal multiple-beam interferometer, there is a simple relation between the height (thickness) of a crystal h and the intensity of the interference image at the corresponding point $(x; y)$:

$$I(h(x;y)) = I_0 \left(1 - \frac{A}{1 - B\cos\varphi(h(x;y))}\right), \tag{22}$$

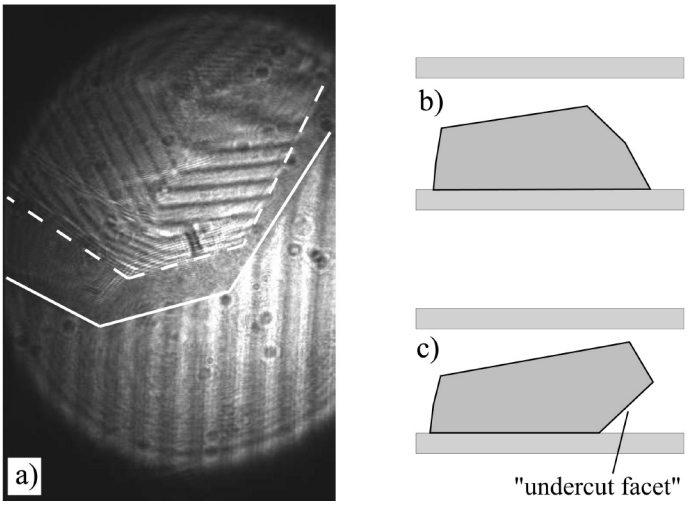

Fig. 7. a) Interferogram of a ^{3}He crystal (in the upper part) at 0.55 mK. The white solid line marks the edge of the crystal. Between the solid and dashed white lines the interference fringes cannot be resolved due to the steep slopes of the crystal surface. Corresponding crystal profile (b) without and (c) with "undercut". For explanation, see text.

where I_0 is the initial intensity, the constants A and B depend on the reflectivities of the two mirrors and the wavefront phase $\varphi = 4\pi\Delta n h/\lambda$. The difference Δn in the refractive indices of solid and liquid ^{3}He is $1.66 \cdot 10^{-3}$ at about 1 mK. In our experimental setup ($\lambda = 632.8$ nm) the corresponding change in the crystal thickness between the two neighboring interference fringes (a phase change of 2π) is 190 μm.

Figure 7a shows an interferogram of a faceted ^{3}He crystal taken during growth. The solid white line is a border line separating the regions in the cell having both liquid and solid (the upper part of the interferogram) and liquid only (the lower part). The main contribution to the background pattern is caused by a liquid helium wedge due to the 2° tilt of the top window of the cell which arises because during adjustments of optics at room temperature there is vacuum in the cell. Additionally to that during cooldown the mirrors of the interferometer became slightly tilted with respect to each other, which also gives a small contribution to the background.

In the interferogram like in Fig. 7a the regions with equidistant and parallel fringes (except the background, of course) correspond to flat surfaces on the crystal, *i.e.*, facets, when the lower part of the crystal is against the bottom window of the cell as illustrated in Fig. 7b. Sometimes "undercut"

crystals (see Fig. 7c) were observed and one such example is presented in the next Section. We want to point out that as the fringes on our interferograms are the "equal thickness" fringes, the corresponding interferograms for the crystal profiles presented in Figs. 7b and 7c should be very similar. However, typically in these questionable regions near the crystal edge the fringes could not be solved as in Fig. 7a between the solid and dashed white lines.

Two different approaches were utilized to image the crystals. Under stable conditions, the phase-shift technique[67,64] was applied (see Section 4.1). In dynamic situations, like during crystal growth, single interferograms were taken which were analyzed using the intensity-based analysis methods[68] (see Section 4.2). The facets were identified by comparing the measured angles between the facets with the theoretically possible ones for the perfect *bcc*-structure. This technique has been widely applied in the crystallography before the development of the X-ray spectroscopy.[40] Of course, there is a big number of facets which are infinitely close to each other and satisfy the selection criteria within experimental precision. In analysis always the most "stable" facet was selected, *i.e.*, the facet with maximum reticular density. The typical difference between the expected and measured angles was 2°; in the worst cases it was around 6° for the shortest fringes.[66]

4.1. Phase-Shift Technique

A single interferogram contains information only on the intensities while the phase of a wavefront is lost. However, the wavefront phase can be directly calculated from the difference in the recorded intensity data when a known phase change is induced by varying the distance between the mirrors in the Fabry-Pérot interferometer.[67]

In the case of multiple-beam interferometry the intensity is determined by four variables: I_0, A, B and φ in Eq. (22). As a result, at least four interferograms of the same crystal with different phase shifts are required to calculate the initial phase φ. In our experiments with the phase-shift technique the crystal surface profile was reconstructed using four subsequent interferograms with a $\pi/2$ phase shift in between; the optical path was changed by applying a high voltage to the piezo crystal. The detailed description of the phase-shift technique and the corresponding data analysis is provided in Ref. 66.

In Figure 8a the measured wavefront phase of the ^{3}He crystal seen in Fig. 7a is presented. We would like to pay attention to a vastly improved contrast of the image as compared with the single interferogram. The non-uniform initial intensity distribution of a single interferogram is canceled

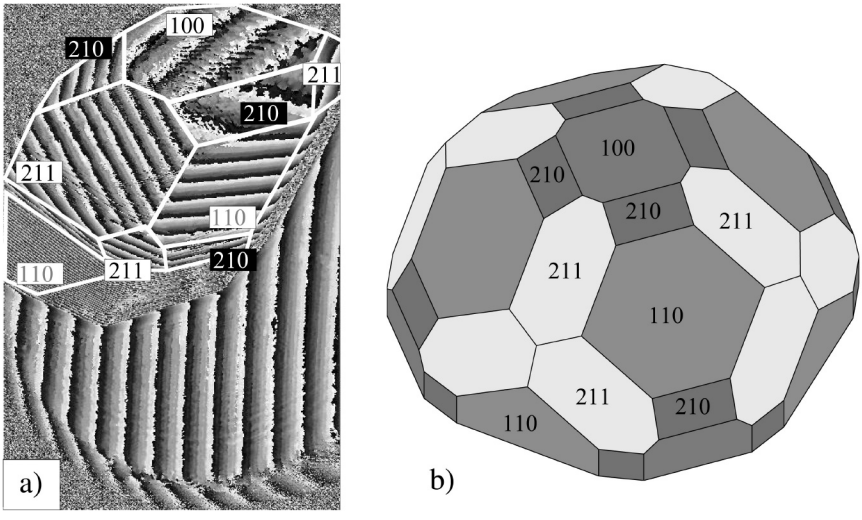

Fig. 8. a) Measured phase of a ^{3}He crystal obtained using the phase-shift technique. Solid white line surrounds the identified facets marked with Miller indices. b) Computer-generated shape of a *bcc*-crystal with four corresponding facet types.

out and the resulting phase has the values ranging between $-\pi$ and π. A continuous change from black to white color corresponds to the increase of the phase (crystal thickness), while a sudden change from white to black color is an artificial phase jump due to the calculation of a reverse cosine function. The phase jumps can be unwrapped by adding or subtracting 2π and the parameters of the facets can be obtained by fitting with a plane. Once the parameters are known the angles between facets (or between their normal vectors) can be calculated and the facets identified after that. The crystal shown in Fig. 8a has four types of facets, (110), (100), (211), and (210). A computer-generated *bcc*-crystal with corresponding facets is shown in Fig. 8b.

Figure 9a shows another example of a ^{3}He crystal observed at 0.55 mK. From the measured phase map one could count that there are seven different facets on the crystal surface. However, careful analysis shows that the crystal has actually five facets on the top surface and some of these facets are undercut with the underlying facet on the lower part of the crystal (see Fig. 7c). The unwrapped phase, corresponding to the thickness profile of the crystal, is shown in Fig. 9b. Black solid lines mark the edges of the identified facets, and black dashed line illustrates the position where the (110) facet on the lower surface of the crystal detaches from the bottom window of the

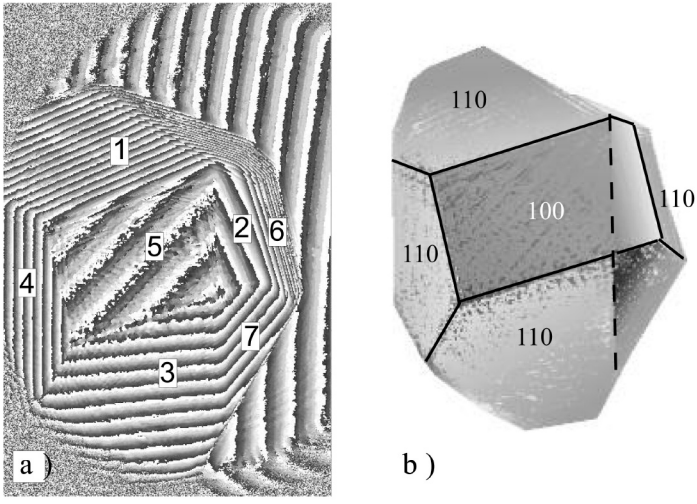

Fig. 9. a) Measured phase of a ^{3}He crystal at 0.55 mK, for explanation of numbered regions, see text. b) Corresponding unwrapped phase, the identified facets are labeled by Miller indices.

cell. Thus the regions 2 and 5 on the phase map in Fig. 9a correspond to the (100) facet and the regions 3 and 7 to the (110) facet, respectively, on the upper surface of the crystal.

The phase-based method is a sensitive and convenient technique to use under small growth/melting rates. The main advantage of that method is a possibility to calculate quickly the thickness plot of the crystal. The restored surface profile of a rounded ^{3}He crystal (during melting) is presented in Ref. 69. However, when crystals are grown/melted at high velocities, this method is of no use because the shape of the crystal varies remarkably during the 20 seconds required to complete one full four-frame measurement with our slow-scan camera. Under such circumstances we have applied the intensity-based analysis methods in order to analyze the single interferograms and these methods are described in the next Section.

4.2. Intensity-Based Analysis Methods

In principle, very sophisticated intensity-based methods could be applied in the analysis to reconstruct the whole shape of a crystal from a single interferogram.[68] However, our goal was to determine only the angles between the facets and in such case the intensity-based methods are simple

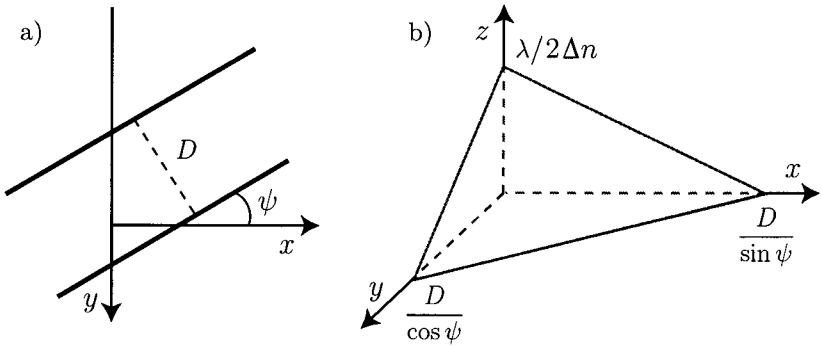

Fig. 10. a) Set of fringes (maxima or minima) belonging to the same facet. b) The plane corresponding to the fringes.

to apply.

Figure 10 shows the principle which was used to calculate the parameters of the facets from the interferograms. The distance between the neighboring fringes equals D and the fringes are tilted by an angle ψ with respect to the x axis (see Fig. 10a). In the case of multiple-beam interferometry the crystal height (thickness) change between two neighboring fringes corresponds to $\lambda/2\Delta n$. The orientation of the facet (plane) in question (see Fig. 10b) is then uniquely determined by the following plane equation:

$$\frac{\sin\psi}{D}x + \frac{\cos\psi}{D}y + \frac{\pm 2\Delta n}{\lambda}z = const, \tag{23}$$

where "$\pm$" is the sign of the thickness change which could be deduced from the fact that the central part of the crystal is higher than its edges or found from the measurements with the phase-shift technique.

We have employed three different methods to find the distance between the fringes and the angle with respect to the horizontal axis. These methods were the Hough technique, fitting with a "corrugated-iron" function and the auto-correlation method.

To obtain the parameters of fringes with the Hough method[70] the positions of the fringe minima (maxima) were located and combined into a skeleton pattern. The example of an interferogram together with the corresponding skeleton is presented in Ref. 32. The Hough technique converts a point on the $(x - y)$ image plane to a unique curve in the $(\rho - \theta)$ plane

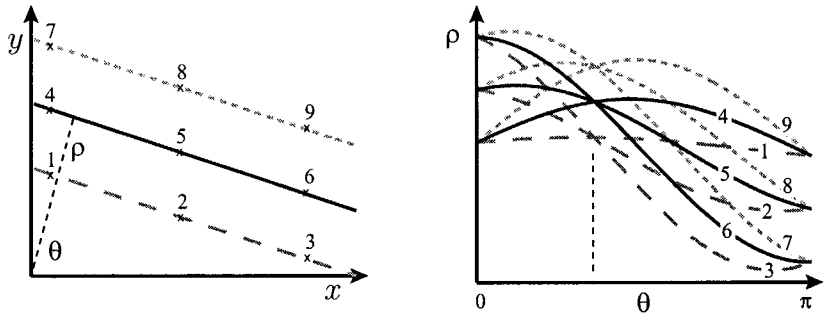

Fig. 11. Hough technique: the set of equidistant parallel lines in left is transformed into curves in right which reveal the slope of the lines and their distance from the origin (see text).

determined by the equation $\rho = x\cos\theta + y\sin\theta$. Thus each line on the $(x-y)$ plane generates a family of sinusoidal curves which all cross the point $(\theta_0;\rho_0)$, where θ_0 is the slope of that line and ρ_0 is the distance from the line to origin (see Fig. 11). The set of parallel equidistant lines will produce a set of cross-points with the same θ_0, while the distance between neighboring points equals to the line spacing D.

The most practical way to find the facet parameters is, however, to fit the intensity distribution of the facet region with a sinusoidal waveform that is stretched out into two dimensions. The real intensity distribution in the majority of cases was not described well with Eq. (22). The main reason for this discrepancy is probably the non-uniform illumination as well as the absorption and dispersion of light which are neglected in the ideal case. The trial function had the same set of fitting parameters as the exact function: the wave number (the inverse distance between the minima), the orientation with respect to the horizontal axis, the phase shift and the amplitude of the intensity oscillations. The changes in mean intensity were determined by appropriate normalization of data. The normals of the facets were found from the obtained values of the wave number and the orientation.

The distance between fringes and the orientation of the corresponding plane were determined by the auto-correlation function as well. The auto-correlation method is often used in the classification of textures, it takes series of adjacent pixels and correlates them with themselves. Marked peaks in the curve indicate a periodicity, and the sizes of the peaks show how predictable the texture is from its periodic repetition.

The results (the measured angles between the facets) obtained by all three methods were very close. The Hough technique is the most sophisti-

cated method and was used only to analyze the crystals with small facets. The fitting with "corrugated-iron" function proved to be the fastest method. However, it easily falls to local minima and was checked with significantly slower auto-correlation function.

4.3. Analysis of the Growth Velocities of Facets

The analysis of the growth sequences was conducted as follows: the interferogram with a crystal with the smallest number of facets (usually the last interferogram of the sequence) was treated first. When the facets on that interferogram were identified and thus the orientation of the crystal determined, the preceding interferogram with more facets was processed and so on. The anisotropy of growth simplified the identification of different regions on the crystal shape, the edges of various facets were traced by looking at animated sequences of interferograms.

The interface velocities were calculated from the movements of the interference fringes between two subsequent interferograms. The cross-correlation function was one of the methods used to trace the displacements of the fringes. The cross-correlation is an analogous to the auto-correlation with the exception that two subsequent images are compared. Another method employed to calculate the interface velocity was to fit a sinusoidal waveform function with only one free parameter, the phase shift.

5. RESULTS

5.1. Nucleation of Crystals

It is commonly known that it is difficult to nucleate and grow only one (single) ^{3}He crystal from the normal liquid. Below $T_m = 320$ mK the negative latent heat of crystallization which is absorbed during the growth of the crystal cools the surrounding liquid. Since the thermal conductivity of the normal liquid is rather poor, the rising temperature gradients in the experimental cell are large. As a result, it becomes favorable to nucleate a new crystal somewhere else in the cell in a warmer spot, rather than continuing the growth of the existing seed. On the other hand, single ^{3}He crystals can be produced relatively easily below $T_N = 0.93$ mK where the surrounding superfluid has good thermal conductivity and the latent heat of crystallization is small.

Our attempts to nucleate crystals in the field of view with laser light pulses (up to 2 minutes long) were not successful. The application of a high

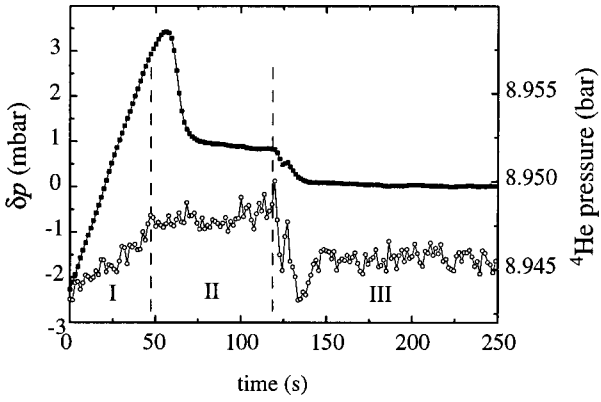

Fig. 12. Pressure traces of ^{3}He (squares) and ^{4}He (circles) before and after the crystal nucleation at 0.78 mK. For details, see text.

voltage to the nucleator in order to enhance the pressure locally by a high electric field did produce a crystal seed in the field of view at a few times lower excess pressure than with the spontaneous nucleation.

Figure 12 presents the pressure trace of one of the spontaneous nucleation events at 0.78 mK. During regions I and II the experimental cell was compressed with a constant mass flow of ^{4}He from the room-temperature ballast volume. The change of slope of the ^{4}He pressure (the beginning of region II) is due to the nucleation of solid ^{3}He. Soon after the appearance the crystal grew rather fast and reduced the excess pressure δp to an almost constant level. After the flow of ^{4}He was stopped (the end of region II) the pressure relaxed towards the equilibrium melting curve value $\delta p = 0$ (region III). For nucleation and for growth of that particular ^{3}He crystal, δp was 2.6 and 0.90 mbar, respectively.

5.2. Observations of Higher Order Facets

We nucleated the ^{3}He crystals typically at the lowest possible temperature. The growth and melting of crystals were taking place at almost constant temperature by compressing or decompressing the cell. The typical pressure trace of a growing ^{3}He crystal is shown in Fig. 13 together with the ^{4}He pressure trace measured at room temperature. In this sequence the crystal was grown with several different ^{4}He flows: in region II the compression rate was twice that in region I and in region III the compression rate was increased further by a factor of 1.7. The full-frame images of the cell

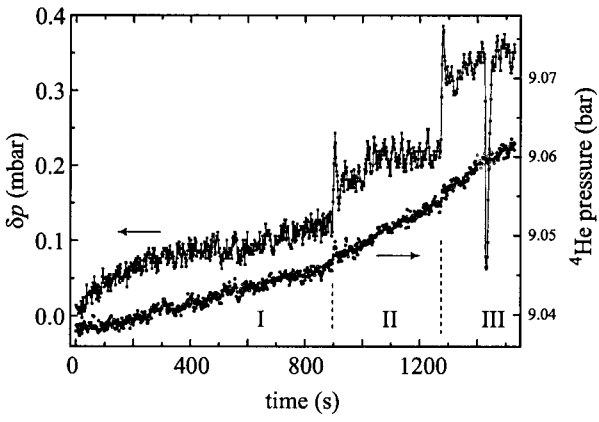

Fig. 13. Excess pressure δp of ^{3}He (squares) for a growing ^{3}He crystal at 0.55 mK. The ^{4}He pressure (circles) is shown on the right axis. The regions I, II and III correspond to the three different compression rates of the cell.

were acquired every 4 seconds.

Some selected interferograms of the growth sequence with the pressure traces in Fig. 13 are presented in Fig. 14. Initially (after melting) the crystal was nicely rounded and had no facets. After starting the slow and steady cell compression, the pressure of ^{3}He increased (region I in Fig. 13) and at the same time the interference fringes started to show corners as seen in Fig. 14b due to the appearance of facets on the crystal surface.

In the initial stage of growth, when the facets were small, we were not able to identify them as we need at least three equally spaced parallel fringes per facet for our analysis.[2] In Figure 14b, 50 seconds after starting the growth, several facets can be clearly identified. The analysis revealed that in the beginning mostly facets with high Miller indices dominated on the surface of the growing crystal and these facets were wedged out later by more slowly growing facets. For example, the facet (411), seen in Fig. 14b, was present on the crystal surface only for about 30 seconds. Other higher order facets, (431), and (321) together with (311), disappeared approximately within 200 s and 400 s after their identification, respectively. In Figure 14f, taken 25 minutes after starting the growth, only three different types of facets, (110), (100) and (211), the most "stable" facets are seen, and these facet types were observed also in the earlier experiments by Wagner *et al.*[24]

[2]Two fringes can as well belong to a cylindrical surface, so three is the smallest number of fringes required to determine and identify a plane.

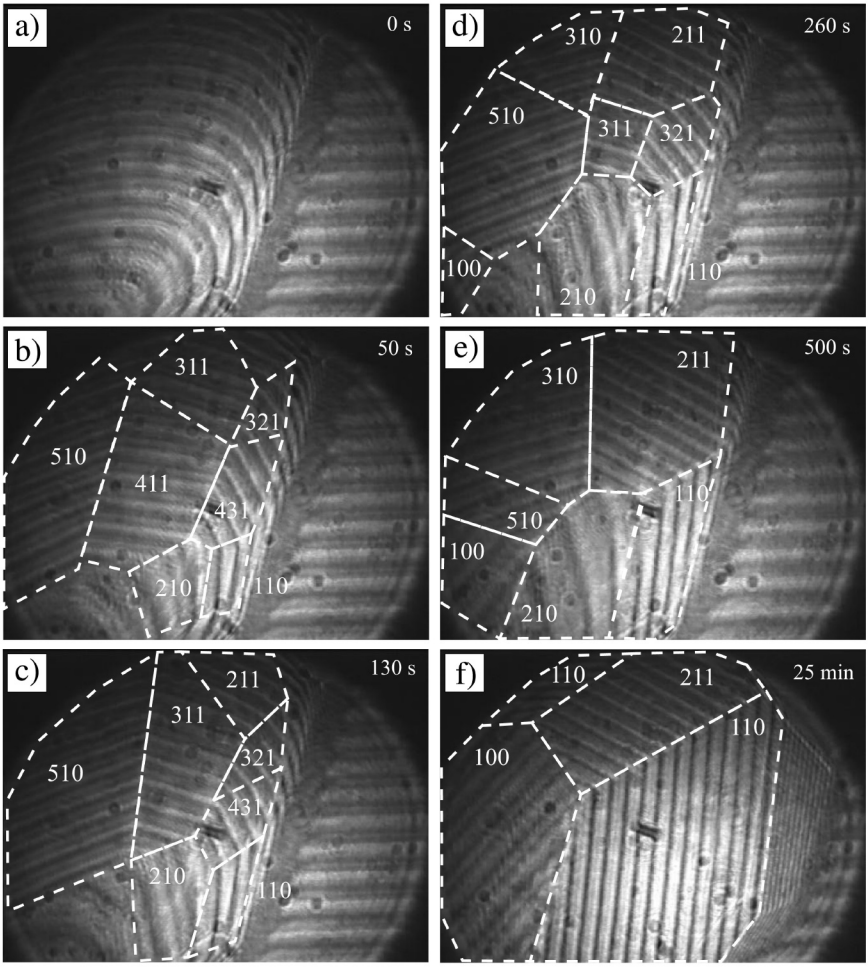

Fig. 14. Sequence of a growing ^{3}He crystal at 0.55 mK. The edges of the facets marked by dashed white lines are not exact, they are shown for clarity.

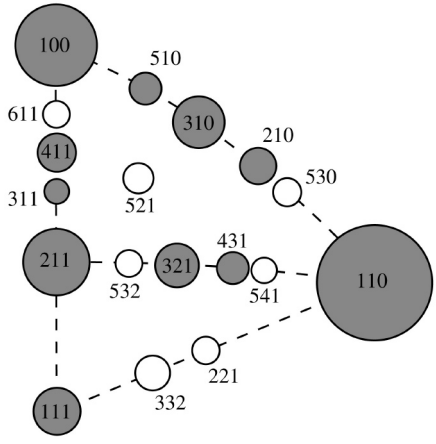

Fig. 15. Elementary patch of a *bcc* crystal with Miller indices of the facets. Filled points represent experimentally observed facets on ^{3}He crystals, empty ones correspond to facets expected to be seen. The diameters of the circles are proportional to the corresponding interplanar distances. The coordinates are exact, looking along the [111] direction.

Most of our growth sequences were started from the rounded shape. In these experiments the same types of facets appeared on the crystal surface and altogether eleven different types of facets were identified. Each facet was detected on more than just one interferogram and all facet types were uniquely identified with the exception of the (510) facet the orientation of which is rather close to the (410) facet. However, as mentioned earlier, in such cases the more "stable" facet type was chosen.

Figure 15 shows the positions of all detected facets on one elementary patch of the crystal habit as filled circles. Also the positions of those facets which were not observed, but have higher (or equal) reticular density and thus higher (or equal) roughening transition temperature than the (311) facet, the highest order facet we did observe, are shown in Fig. 15 as open circles. The sequence of facets: (100), (510), (310), (210) and (110) forms a precursor to the "devils' staircase" (see Section 2.1), which is expected to appear on the crystal surface in the case of a long-range repulsive step-step interaction.[35]

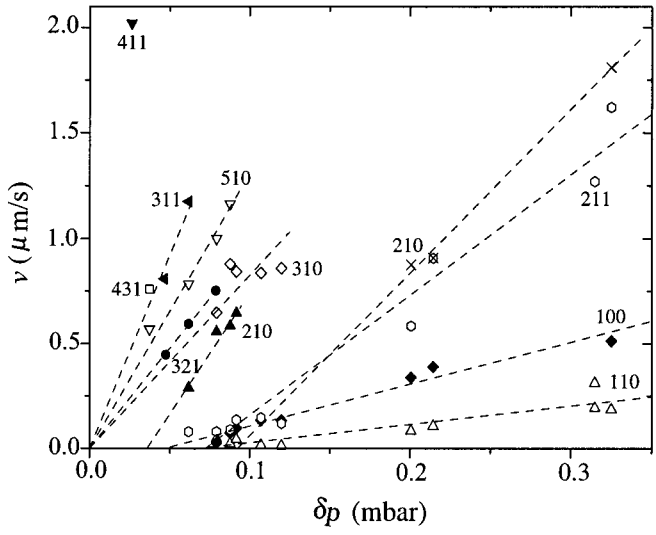

Fig. 16. Growth anisotropy of a ^{3}He crystal at 0.55 mK. The dashed lines are linear fits to the data for different facets marked with Miller indices.

5.3. Growth Anisotropy of Crystals

From the growth sequence, presented in the previous Section, we were able to extract the velocities of most of the observed facets. The measured growth rates of facets with the corresponding overpressures are presented in Fig. 16. The observed anisotropy is rather strong, the velocities of the (110) and the (510) facets, for instance, differ by approximately one order of magnitude. The measured growth velocities show a linear dependence on the applied overpressure, which suggests that the growth mechanism is spiral growth in the regime of the so called suppressed step mobility [see Eq. (21)].

Using Eq. (21), the step free energies of the facets can be calculated from the measured facet velocities because the only value which is not strictly defined in that equation is the number of elementary steps produced by dislocations on the higher order facets. The actual distribution of dislocations in the crystal and their types are not known. However, the most "stable" facets grow slowly, have larger sizes, and are present for a longer time on the crystal surface. As a result, these facets should be observed in experiments. Thus in our analysis we assumed that one dislocation produces one step since the corresponding growth velocity is the slowest. For the critical

Table 1. Miller indices of the experimentally observed facets, their reciprocal lattice vectors $\langle hkl \rangle$, the interplanar distance ratios with respect to the (110) facet, the measured free energies of the elementary step β and the highest temperatures $T_{\rm obs}^{\rm max}$ at which the corresponding facet has been observed.

Facet type	$\langle hkl \rangle$	$(d_{110}/d_{hkl})^2$	β (erg/cm)	$T_{\rm obs}^{\rm max}$ (mK)
110	$\langle \frac{1}{2}\ \frac{1}{2}\ 0 \rangle$	1	$6.6 \cdot 10^{-10}$	100
100	$\langle 1\ 0\ 0 \rangle$	2	$1.4 \cdot 10^{-10}$	10
211	$\langle 1\ \frac{1}{2}\ \frac{1}{2} \rangle$	3	$3.3 \cdot 10^{-11}$	<10
310	$\langle 1 \frac{1}{2}\ \frac{1}{2}\ 0 \rangle$	5	$1.4 \cdot 10^{-11}$	0.55
111	$\langle 1\ 1\ 1 \rangle$	6	—	0.55
321	$\langle 1 \frac{1}{2}\ 1\ \frac{1}{2} \rangle$	7	$8.6 \cdot 10^{-12}$	0.55
411	$\langle 2\ \frac{1}{2}\ \frac{1}{2} \rangle$	9	$8 \cdot 10^{-13}$	0.55
210	$\langle 2\ 1\ 0 \rangle$	10	$7.0 \cdot 10^{-12}$	0.55
210	$\langle 2\ 1\ 0 \rangle$	10	$4.9 \cdot 10^{-12}$	0.55
510	$\langle 2 \frac{1}{2}\ \frac{1}{2}\ 0 \rangle$	13	$3.4 \cdot 10^{-12}$	0.55
431	$\langle 2\ 1 \frac{1}{2}\ \frac{1}{2} \rangle$	13	$2.2 \cdot 10^{-12}$	0.55
311	$\langle 3\ 1\ 1 \rangle$	22	$1.4 \cdot 10^{-12}$	0.55

velocity we used $v_c = 7$ cm/s (see Section 2.2.2). Table 1 lists all observed facets with their step free energies.

5.4. The Step Energies of Facets

Figure 17 shows the calculated step free energies plotted versus the step height in log-log coordinates. A linear fit is consistent with the data and gives a fourth order power dependence, as predicted by the strong-coupling model, Eq. (8). The best fit is $\beta = 6.5 \cdot 10^{20} d^4$ erg/cm^5. The obtained result suggests that the step-step interactions are of elastic origin (r^{-2}).[41] Using the estimated value for the Young modulus of *bcc* ^{3}He, $E = 10^8$ dyne/cm^2, we get for the elastic strain force $f = 0.1...0.2$ erg/cm^2, which is higher but of the same order of magnitude as the value of the surface stiffness, as expected. However, as was pointed out in Section 2.1.1, the strong-coupling model is not expected to be valid for primary facets like (110), (100) and (211). Thus we have plotted our data also in a semilog plot, suggested by Eq. (9), as shown in Fig. 18.

Using a fit for the three most stable facets one obtains $\beta = 0.63\ d \cdot \exp(-l/2d)$ erg/cm^2 with $l = 2.0 \cdot 10^{-7}$ cm $\approx 6.6\ d_{110}$ from Fig. 18. This value of l is consistent with our estimate obtained with ^{4}He from the β_{0001} value

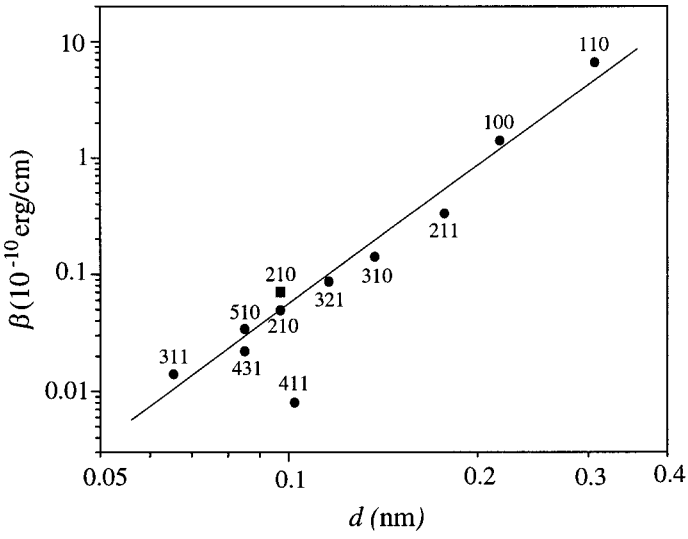

Fig. 17. The step free energies of different facets on a ^{3}He crystal at 0.55 mK. The solid line is a linear fit with a slope of 3.95 ± 0.5.

as discussed in Section 2.1.2. But the prefactor gives a value for the surface stiffness of 0.50 erg/cm^2 which is a factor of 8 higher than the experimental value.[73] Since the strong- and the weak-coupling models are supposed to be valid for the higher order and the primary facets, respectively, we describe our data with a sum of Eq. (8) and Eq. (9)

$$\beta_{\text{sum}} = c_1 d^4 + c_2 d \exp(-c_3/d). \tag{24}$$

A nonlinear fitting procedure gives too much weight to the highest points and we have fixed $c_1 = 4.5 \cdot 10^{20}$ erg/cm^5 by using only the highest order facets. Then the best fit gives for the value of $c_3 = 9 \cdot 10^{-8}$ cm or $l = 6\ d_{110}$, while $c_2 = 0.15$ erg/cm^2. The result is shown in Fig. 18 as the solid line. Thus the values obtained by fitting are in agreement with the expectations, but it is clear that more experiments are still required.

The free energy β of the elementary step on the (110) facet equals to $6.6 \cdot 10^{-10}$ erg/cm and this value is, unexpectedly, almost the same as has been measured in ^{4}He for the (0001) facet. The width of the elementary step ξ_{110} calculated using Eq. (10) and Eq. (2) equals to $\xi_{110} \approx 2\ d_{110}$ which is about 4 times smaller than the step width on the (0001) facet in ^{4}He. In ^{4}He, the coupling of the interface to the lattice has been reported to be weak,[7] however, in spite of the predictions of even weaker coupling in ^{3}He,[18]

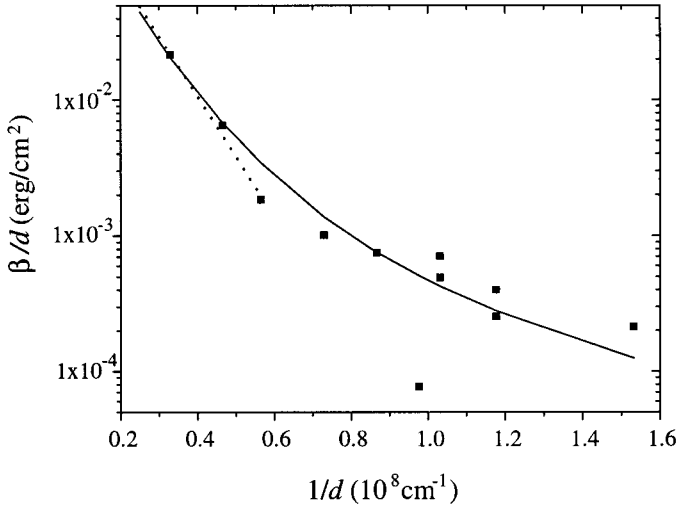

Fig. 18. The step free energies of different facets on a ^{3}He crystal at 0.55 mK presented on a semilog plot of β/d versus the inverse step height $1/d$. The dotted line is a fit according to Eq. (9) to the three highest points. The solid line is a fit according to Eq. (24), as discussed in the text.

according to our results this coupling is actually stronger in ^{3}He than in ^{4}He.

Using Eq. (11) with the measured surface stiffness[22] $\gamma_0 = 0.06$ erg/cm^2 and the obtained step energies it is easy to estimate the equilibrium sizes of the facets: the equilibrium size of the (110) facet should be approximately $1/3\ R$ and higher order facets are expected to be smaller. It means that within our optical resolution the (110) facets could have been detected in equilibrium. And indeed, in our experiments we have seen, after the growth of a crystal was stopped, that the edges between facets rounded off, indicating the relaxation toward equilibrium. Unfortunately, this cannot only be attributed to the equilibrium crystal shape since the reverse happens when we stopped melting of the crystal. Thermal effects in the filling line are responsible for such pressure instabilities. In order to measure the real equilibrium shape of the ^{3}He crystal a cold valve should be installed into the ^{4}He fill line in our present setup.

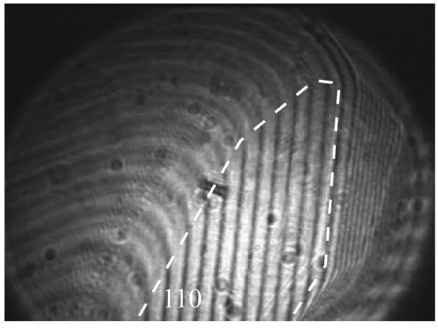

Fig. 19. The (110) facet (surrounded with white dashed line) present on the surface of ^{3}He crystal during melting at 0.55 mK.

5.5. Growth Rate of Rough Surfaces

The measurement of the growth rate of a ^{3}He crystal during melting is rather difficult at $T < T_N$. Our experience in that respect is similar to what is described by Nomura *et al.*[28] and by Akimoto *et al.*[29] The melting rate is fast and the measurement technique to record the changes (NMR or optical imaging) is rather slow. So either we can only apply a very small negative driving force ("underpressure"), which then is not precise, or the crystal changes its shape, size and interface area significantly between two recorded interferograms. The analysis shows that the crystal initially melts very fast near the edges between facets and after the sharp edges have disappeared, surfaces with smaller and smaller curvature become involved in melting. As an example, Fig. 19 shows an interferogram of a melting crystal, the dashed line highlights the (110) facet still present during melting.

The average velocity of melting, measured at 0.55 mK, was 1.67 μm/s with the corresponding underpressure of $\Delta p = -11.3$ μbar. This yields an effective growth coefficient $k_{\text{eff}} = 2 \cdot 10^{-3}$ s/m. Note that the measured growth rate of the fastest facet (411) we observed, was two times smaller than that of melting. This corroborates our assumption that the growth of (most of) the facets was not determined by dissipative processes in the bulk phases, but reflects the intrinsic mechanisms taking place at the crystal surface. It is interesting to compare our result on the effective growth coefficient k_{eff} at $T = 0.55$ mK in zero magnetic field with earlier measurements, which were obtained in a small magnetic field. The results are given in Table 2.

According to the data in Table 2, within the u2d2 phase the magnetic field dependence of the effective growth coefficient seems to be weak, which is as expected for growth that is mostly determined by bulk properties.[72]

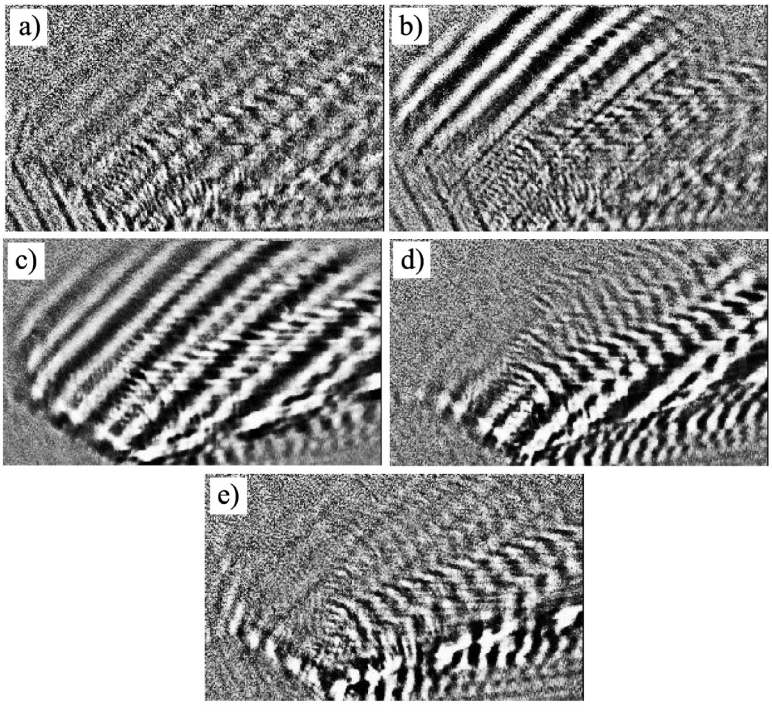

Fig. 20. Step-like growth of the (100) facet. During 8 seconds crystal has grown about 60 μm.

Probably most of the magnetic field dependence is in the latent heat, which changes significantly only when the magnetic field is high enough for the solid to go through the phase transition into the high field phase at $B \approx 0.45$ T.

We also would like to report on a very special feature: the creation of a macroscopic step propagating on the (100) facet. Figure 20 shows the subtractions of the successive interferograms during the observed step-like growth. The images in Fig. 20, a and e, correspond to typical difference-interferograms obtained during (slow) growth of the (100) facet. A sudden change of the growth rate is easily observed in Fig. 20b, in which the step covers half of the facet. During the next frame, Fig. 20c, it expands over the whole facet, and starts to disappear on Fig. 20d.

The profile of the moving step is expected to be similar to the one illustrated in Fig. 3. The difference-interferogram in Fig. 20c indicates that the width of the step was about 3 mm. The analysis showed that only the (100) facet was growing and it gained about 60 μm of height in approximately

Table 2. The effective growth rate of solid ^{3}He in the antiferromagnetically ordered u2d2 phase, as determined during melting at various temperatures and magnetic fields. We have used the data points only at the lowest temperature of Kawaguchi *et al.*[30]

Temperature (mK)	Magnetic field (T)	$k_{\rm eff}$ (s/m)	Reference
0.55	0	$2 \cdot 10^{-3}$	this work
0.7	0.2	$2.3 \cdot 10^{-4}$	[29]
0.73	0.07	$5 \cdot 10^{-4}$	[28]
0.7	0.33	$4 \cdot 10^{-4}$	[30]
0.62	0.33	$6 \cdot 10^{-4}$	[30]

8 seconds.

The pressure trace during this burst-like growth phenomenon corresponds to the sharp dip depicted in Fig. 13. The sudden pressure drop indicates the creation of the defect and the fact that a significantly lower overpressure is required to drive the growth of the rough surface. During the burst-like growth the overpressure was constant at $\delta p = 65$ μbar. The cell compression rate of $5.3 \cdot 10^{-5}$ cc/s is in a good agreement with the volume change of the crystal. The obtained effective growth coefficient equals to $3 \cdot 10^{-3}$ s/m, which is close to the value obtained during melting. This may reflect the fact that the growth coefficient of a rough surface is mostly determined by bulk properties [the second term in Eq. (15)].

6. CONCLUSIONS

To summarize, single ^{3}He crystals were grown and studied at our lowest temperature of 0.55 mK using a multiple-beam interferometer. Altogether eleven different types of facets were identified during crystal growth by applying advanced methods of the interferogram analysis while earlier only three different types had been observed.

The growth rates of faceted and rough surfaces of ^{3}He crystals were measured. The growth and melting velocities of rough surfaces were not intrinsic, but determined by the latent heat and the bulk properties of the liquid and solid. The results are consistent with earlier measurements at somewhat higher temperatures and the average effective growth coefficient $k_{\rm eff}$ equals to $2 \cdot 10^{-3}$ s/m at $T = 0.55$ mK. Unfortunately, it is difficult to compare this value with previous measurements[29,28,30] due to the dependence

on the experimental cell geometry.

The smooth (faceted) surfaces were growing by approximately an order of magnitude slower than the rough surfaces. We were able to measure the anisotropy of the growth kinetics for ten types of facets. The obtained linear dependence of the growth rates on the driving force points to spiral growth with limited step mobility. Most probably the critical step velocity is due to the Cherenkov emission of magnons.

We obtained the free energies of steps β for ten observed facets. The fourth power dependence on the elementary step height, $\beta \propto d^{3.9\pm0.5}$, indicates that the step-step interactions have an elastic origin. The values for the step free energy and the width of the elementary step of the most stable (110) facet, $\beta_{110} = 6.6 \cdot 10^{-10}$ erg/cm and $\xi_{110} = 2...3\ d$, when compared with the corresponding values for the (0001) facet in ^{4}He, show that the coupling of the interface to the crystal lattice in ^{3}He is stronger than in ^{4}He. If we express the strength of the coupling with the parameter $\beta/\gamma d$ (see Introduction), we find $\beta/\gamma d = 0.36$ for ^{3}He, while the value 0.057 has been obtained for ^{4}He.[20] The measured values for β suggest that the critical overpressure for dynamic roughening in ^{3}He (see Section 2.1.2) is rather high for the facets we observed, at least several mbar.

The above analysis shows that in order to produce and observe more new facets in ^{3}He one should have a good optical and time resolution and be very careful in choosing the suitable growth regime. It is also clear that direct measurements on the equilibrium crystal shape and the actual roughening transition temperatures are necessary in ^{3}He.

ACKNOWLEDGMENTS

We would like to thank S. Balibar, V. Eltsov, J.P.H. Härme, K. Keshishev and G. Tvalashvili for help and useful discussions. This work was supported by the ULTI II (ERB FMGE CT98 0122) and ULTI III (HPRI-1999-CT-00050) grants of the European Union and the Academy of Finland [Finnish Centre of Excellence Programme (2000-2005)] and by INTAS grant 96-610.

REFERENCES

[a] Present address: Department of Physics, Stanford University, Stanford, CA 94305-4060, USA.

[b] Present address: Department of Physics and Astronomy, University of New Mexico, 800 Yale Boulevard NE, Albuquerque NM 87131, USA.

1. J.C. Heyraud and J.J. Métois, *J. Cryst. Growth* **82**, 269 (1987).
2. J. Lapujoulade, J. Perreau, and A. Kara, *Surface Science* **129**, 59 (1983).
3. C. Rottman, M. Wortis, J.C. Heyraud, and J.J. Métois, *Phys. Rev. Lett.* **52**, 1009 (1984).
4. K.A. Jackson and C.E. Miller, *J. Cryst. Growth* **40**, 169 (1977).
5. M. Elbaum, *Phys. Rev. Lett.* **67**, 2982 (1991).
6. W.K. Burton, N. Cabrera and F.C. Frank, *Philos. Trans. R. Soc. London* **243A**, 299 (1951).
7. P. Nozières, in *Solids Far From Equilibrium*, ed. C. Godrèche (Cambridge University Press, Cambridge, 1991).
8. K.O. Keshishev, A.Ya. Parshin, and A.V. Babkin, *JETP Lett.* **30**, 56 (1979).
9. A.Ya. Parshin, in *Low Temperature Physics*, ed. A.S. Borovik-Romanov (MIR Publishers, Moscow, 1985) and references therein.
10. S. Balibar and P. Nozières, *Solid State Comm.* **92**, 19 (1994) and references therein.
11. J.E. Avron, L.S. Balfour, C.G. Kuper, J. Landau, S.G. Lipson, and L.S. Schulman, *Phys. Rev. Lett.* **45**, 814 (1980).
12. S. Balibar and B. Castaing, *J. Physique Lett.* **41**, L-329 (1980).
13. J. Landau, S.G. Lipson, L.M. Määttänen, L.S. Balfour, and D.O. Edwards, *Phys. Rev. Lett.* **45**, 31 (1980).
14. K.O. Keshishev, A.Ya. Parshin, and A.V. Babkin, *JETP* **53**, 362 (1981).
15. P.E. Wolf, S. Balibar, and F. Gallet, *Phys. Rev. Lett.* **51**, 1366 (1983).
16. J.P. Ruutu, P.J. Hakonen, A.V. Babkin, A.Ya. Parshin, and G. Tvalashvili, *J. Low Temp. Phys.* **112**, 117 (1998).
17. P. Nozières and F. Gallet, *J. Physique* **48**, 353 (1987).
18. S. Balibar, F. Gallet, F. Graner, C. Guthmann, and E. Rolley, *Physica* **B 169**, 209 (1991) and references therein.
19. L. Vitos, A.V. Ruban, H.L. Skriver and J. Kollár, *Surface Science* **411**, 186 (1998); L. Vitos, H.L. Skriver and J. Kollár, *Surface Science* **425**, 212 (1999).
20. E. Rolley, E. Chevalier, C. Guthmann, and S. Balibar, *J. Low Temp. Phys.* **99**, 851 (1995).
21. V. Tsepelin, J.P. Saramäki, A.V. Babkin, P.J. Hakonen, J.J. Hyvönen, R.M. Luusalo, A.Ya. Parshin and G.K. Tvalasvili, *Phys. Rev. Lett.* **83**, 4804 (1999).
22. E. Rolley, S. Balibar, F.Gallet, F. Graner, and C. Guthmann, *Europhys. Lett.* **8**, 523 (1989).
23. F. Graner, S. Balibar, and E. Rolley, *J. Low Temp. Phys.* **75**, 69 (1989).
24. R. Wagner, S.C. Steel, O.A. Andreeva, R. Jochemsen, and G. Frossati, *Phys. Rev. Lett.* **76**, 263 (1996); R. Wagner, Ph.D. Thesis, Leiden University (1995).
25. A.F. Andreev and A.Ya. Parshin, *JETP* **48**, 763 (1978).
26. E. Rolley, S. Balibar, and F.Gallet, *Europhys. Lett.* **2**, 247 (1986).
27. Y.P. Feng, Ph.D. thesis, Stanford University, 1991.
28. R. Nomura, H.H. Hensley, T. Matsushita, and T. Mizusaki, *J. Low Temp. Phys.* **94**, 377 (1994).
29. H. Akimoto, R.v. Rooijen, A. Marchenkov, R. Jochemsen, and G. Frossati, *Physica* **B 255**, 19 (1998).
30. Y. Kawaguchi, T. Ueno, Y. Kinoshita, Y. Sasaki and T. Mizusaki, *J. Low Temp.*

Phys. **126**, 27 (2002); also Y. Kawaguchi and T. Mizusaki, *LT23 Proceedings*, to be published.
31. T. Ueno, Y. Kawaguchi, Y. Kinoshita, Y. Sasaki and T. Mizusaki, *J. Low Temp. Phys.* **127**, 1 (2002).
32. V. Tsepelin, H. Alles, A. Babkin, J.P.H. Härme, R. Jochemsen, A.Ya. Parshin, and G. Tvalashvili, *Phys. Rev. Lett.* **86**, 1042 (2001).
33. H. Alles, V. Tsepelin, A. Babkin, R. Jochemsen, A.Ya. Parshin, and I.A. Todoshchenko, *J. Low Temp. Phys.* **124**, 189 (2001).
34. V. Tsepelin, H. Alles, A. Babkin, R. Jochemsen, A. Ya. Parshin, and I.A. Todoshchenko, *Phys. Rev. Lett.* **88**, 045302 (2002).
35. C. Herring, *Structure and properties of solid surfaces*, ed. R. Gomer, C.S. Smith (Univ. of Chicago Press, 1953).
36. L.D. Landau, *Collected Papers* (Pergamon Press, Oxford, 1971).
37. D.S. Fisher and J.D. Weeks, *Phys. Rev. Lett.* **50**, 1077 (1983).
38. S.V. Iordanskii and S.E. Korshunov, *JETP Lett.* **38**, 655 (1983).
39. E. Fradkin, *Phys. Rev.* **B 28**, 5338 (1983).
40. F.C. Philips, *An introduction to Crystallography* (Longmans, New York, 1960).
41. V.I. Marchenko and A.Ya. Parshin, *JETP* **52**, 129 (1980).
42. Y. Akutsu, N. Akutsu and T. Yamamoto, *Phys. Rev. Lett.* **61**, 424 (1988).
43. Note that the considerations here are valid for $N \gg 1$. The real step heights for the observed facets are given in Table 1.
44. S. Balibar, C. Guthmann and E. Rolley, *J. Phys. I France* **3**, 1475 (1993).
45. We want to note that in our previous work, Ref. 32, there is a misprint that $l/d_{0001} = 2.5$.
46. See also F. Pederiva *et al.*, *Phys. Rev. Lett.* **72**, 2589 (1994), who find $l/d \approx 4$ in ^{4}He with a variational Monte Carlo simulation of the liquid/solid interface. Unfortunately the calculation is only done for the (100) surface of the *fcc* structure.
47. A.A. Chernov, *Modern Crystallography III: Crystal Growth* (Springer-Verlag, 1984).
48. B. Castaing and P. Nozières, *J. Physique* **41**, 701 (1980); S. Balibar, D.O. Edwards and W.F. Saam, *J. Low Temp. Phys.* **82**,119 (1991).
49. J. Amrit and J. Bossy, *J. Low Temp. Phys.* **92**, 415 (1993).
50. P.E. Wolf, F. Gallet, S. Balibar and E. Rolley, *J. Physique* **46**, 1987 (1985).
51. F. Gallet, S. Balibar and E. Rolley, *J. Physique* **48**, 369 (1987).
52. M. Uwaha, *J. Low Temp. Phys.* **52**, 15 (1983).
53. A.Ya. Parshin, *J. Low Temp. Phys.* **110**, 133 (1998).
54. S.N. Fisher, G.R. Pickett, and R.J. Watts-Tobin, *J. Low Temp. Phys.* **83**, 225 (1991).
55. D.D. Osheroff and C. Yu, *Phys. Lett.* **77**, 458 (1980).
56. Y.P. Feng, P. Shiffer, D.D. Osheroff, and M.C. Cross, *J. Low Temp. Phys.* **90**, 475 (1993).
57. R. Wagner, P.J. Ras, P. Remeijer, S.C. Steel, and G. Frossati, *J. Low Temp. Phys.* **95**, 715 (1994).
58. A. J. Manninen, J. P. Pekola, G. M. Kira, J. P. Ruutu, A. V. Babkin, H. Alles, and O. V. Lounasmaa, *Phys. Rev. Lett.* **69**, 2392 (1992); H. Alles, J. P. Ruutu, A. V. Babkin, P. J. Hakonen, A. J. Manninen, and J. P. Pekola, *Rev. Sci.*

Instrum. **65**, 1784 (1994).
59. Manufactured by Oxford Instruments, Oxfordshire, OX8 1TL, UK.
60. Stycast 1266 (transparent), manufactured by Emerson and Cummings, Canton, Massachusets, 02021, USA.
61. G.C. Straty and E.D. Adams, *Rev. Sci. Instr.* **40**, 1393 (1969).
62. Andeen-Hagerling 2500A, Andeen-Hagerling, Inc., 31200 Bainbridge Rd., Cleveland, Ohio 44139-2231, USA.
63. W. Ni, J.S. Xia, E.D. Adams, P.S. Haskins, and J.E. McKisson, *J. Low Temp. Phys.* **101**, 305 (1995).
64. J.P.H. Härme, H. Alles, A. Babkin, R. Jochemsen, A.Ya. Parshin, V. Tsepelin, and G. Tvalashvili, *Physica* **B 284-288**, 349 (2000).
65. Star 1 camera by Photometrics, Tucson, Arizona, USA.
66. V. Tsepelin, H. Alles, A. Babkin, J.P.H. Härme, R. Jochemsen, A.Ya. Parshin, and G. Tvalashvili, *J. Low Temp. Phys.* **121**, 695 (2000).
67. G. Bönsch and H. Böhme, *Optik* **82**, 161 (1989).
68. D.W. Robinson and G.T. Reid, *Interferogram Analysis* (IOP Publishing Ltd., 1993).
69. V. Tsepelin, H. Alles, A. Babkin, J.P.H. Härme, R. Jochemsen, A.Ya. Parshin, and G. Tvalashvili, *Physica* **B 284-288**, 351 (2000).
70. J. Illingworth and J. Kittler, *Computer Vision, Graphics, and Image Processing* **44**, 87 (1988).
71. D. Greywall, *Phys. Rev. B* **11**, 1070 (1975).
72. R. van Rooijen, H. Akimoto, R. Jochemsen and G. Frossati, *Physica B* **284-288**, 353 (2000).
73. The prefactor $4/\pi$ was taken into account.[44]